UNIVERSITY
INSTITUTE
OF LISBON

Design of Millimeter Wave TransmitArrays using High Permittivity 3D-Printed Materials

Duarte Alexandre Cabral Barbosa

Master in Telecommunications and Computer Engineering

Supervisor:
Phd, *Sérgio de Almeida Matos*, *Associate* Professor with Aggregation,
Iscte – Instituto Universitário de Lisboa

October, 2025

TECHNOLOGY
AND ARCHITECTURE

Department of Information Science and Technology

Design of Millimeter Wave TransmitArrays using High Permittivity 3D-Printed Materials

Duarte Alexandre Cabral Barbosa

Master in Telecommunications and Computer Engineering

Supervisor:
Phd, *Sérgio de Almeida Matos*, *Associate* Professor with Aggregation,
Iscte – Instituto Universitário de Lisboa

October, 2025

To my family

Acknowledgment

This section is to thank everyone who supported me making this dissertation. I would to highlight and thank Professor Sérgio Matos for the constant guidance, mentoring and expertise throughout this work. I would like to also mention Iscte-Instituto Universitário de Lisboa for all the knowledge that was lectured by professors during my academic journey and to all people involved in this institution that were always ready to assist. My deepest gratitude to Instituto de Telecomunicações (IT) for providing all the necessary tools needed to accomplish this work. Finally, a special thanks for my family and friends who were always an important support during this dissertation.

Resumo

O rápido crescimento das tecnologias de ondas milimétricas (MMW) tem impulsionado a procura de antenas compactas, eficientes e de baixo custo, adequadas para comunicações de banda larga. As antenas metamateriais do tipo *TransmitArray (TA)* surgem como alternativas promissoras às soluções tradicionais, oferecendo elevado ganho, baixas perdas e facilidade de integração. Os recentes avanços na fabricação aditiva (AM) permitem facilitar a implementação destas antenas com materiais dielétricos de baixo custo. Esta tecnologia permite explorar geometrias não convencionais para controlar as propriedades eletromagnéticas da antena.

Esta dissertação centra-se na implementação de TAs de baixo custo com recurso a AM. O objetivo deste trabalho é explorar a nova geração de materiais comerciais de elevada permitividade de forma a reduzir significamente o perfil da antena e permite soluções mais compactas e eficientes. O trabalho inicia-se com o estudo da manipulação de fase com estruturas dielétricas simples, estabelecendo a relação entre a geometria e permitividade do material. A partir destes princípios, foram desenvolvidos dois tipos de antenas: i) um TA para colimação de um sistema focal com desvio; ii) uma antenna com seguimento mecânico baseado no conceito *Risley Prism*.

Os resultados obtidos demonstram que os materiais de elevada permitividade são uma alternativa para implementar antennas TA permitindo combinar o baixo perfil de soluções baseadas em Printed Circuit Board (PCB), com a elevada largura de banda associada a soluções dielétricas e a versatilidade da AM.

Palavras Chave: *Antenas dielétricas*, *TA*, *Materiais de elevada permitividade*, *AM*, *Antenas MMW*.

Abstract

The rapid growth of Millimeter Wave (MMW) technologies has driven the demand for compact, efficient, and low cost antennas suitable for broadband communications. Metamaterial antennas of the TA type emerge as promising alternatives to traditional solutions, offering high gain, low losses, and ease of integration. Recent advances in Additive Manufacturing (AM) facilitates the implementation of these antennas with low cost dielectric materials. This technology allows the exploration of unconventional geometries to control the electromagnetic properties of the antenna.

This dissertation focuses on the implementation of low cost TAs using AM. The objective of this work is to explore the new generation of commercial high permittivity materials in order to significantly reduce the antenna profile and enable more compact and efficient solutions. The work begins with the study of phase manipulation with simple dielectric structures, establishing the relationship between the geometry and permittivity of the material. Based on these principles, two types of antennas were developed: i) a TA for collimating a focal system with a tilt; ii) an antenna with mechanical tracking based on the Risley Prism concept. The results obtained demonstrate that high permittivity materials are an alternative for implementing TA antennas, allowing the low profile of PCB based solutions to be combined with the high bandwidth associated with dielectric solutions and the versatility of AM.

KEYWORDS: *Dielectric antennas*, *TA*, *High permittivity materials*, *AM*, *MMW antennas*.

Contents

Acknowledgment iii

Resumo v

Abstract vii

List of Figures xi

List of Tables xiii

List of Acronyms xv

List of Symbols xvii

Chapter 1. Introduction 1
1.1. Motivation and Context 1
1.2. Objectives 1
1.3. Dissertation Structure 2
1.4. Contributions 2

Chapter 2. State of the Art 3
2.1. Millimeter Wave Antennas 3
2.2. Lens Antennas 4
2.2.1. Material Permittivity in Lens Antennas 5
2.2.2. Dielectric Lens Antennas 6
2.2.3. Geodesic Lenses 8
2.2.4. TransmitArrays 9
2.3. Feeds for Lens Antennas 10
2.3.1. Spatial Feeds 10
2.3.2. Leaky Wave Feeds 11
2.3.3. Integrated Feeds 13
2.4. Metasurfaces 13
2.5. Additive Manufacturing 14

Chapter 3. Design Methodology of Dielectric TA 17
3.1. UC and TA Design 17
3.2. Slab Model 20
3.3. Lens Design with variable height UC 23
3.4. Zoned Lens 31

Chapter 4. Design high permittivity TA 37
4.1. UC Design 37
4.2. TA Design 40
4.3. Risley Prism Implementation 42
4.4. Comparative Analysis of Proposed Designs with other Dielectric based TAs 47

Chapter 5. Conclusion and Future Work 49
Future Work 49

References 51

List of Figures

2.1 Example of a dielectric lens antenna [15]. 6

2.2 Examples of dielectric lens classes: (a) Inhomogeneous and (b) Homogeneous. 7

2.3 Illustration of a geodesic lens concept. The curved metallic surface guides electromagnetic waves along paths equivalent to those in a graded-index dielectric lens [20]. 8

2.4 Example of a TA, with a 3-D printed stand for the Lens and the feed horn [21]. 9

2.5 Illustration of a spatial-feed antenna system, taken from [26] 11

2.6 Fabricated RLSA antenna used for leaky-wave radiation studies, taken from [28]. 12

2.7 Example of an integrated feed antenna system, taken from [4] "ILA fed by a planar self-complementary log-periodic feed". 13

3.1 Homogenized representation of a dielectric UC [21]. 18

3.2 Single dielectric slab model with transmitter (Port 2), receiver (Port 1), and slab height h. 20

3.3 Simulated absolute phase response for different slab heights h. 22

3.4 Simulated transmission for different slab heights h. 23

3.5 Continuous lens model implemented in CST. 24

3.6 Radiation pattern of the continuous lens. 25

3.7 Discrete lens designed with $\varepsilon_r = 7.5$ using $\lambda/2$ discretization, showing the horn feed and lens geometry. 25

3.8 Discrete lens designed with $\varepsilon_r = 7.5$ using $\lambda/4$ discretization, showing the horn feed and lens geometry. 26

3.9 Discrete lens designed with $\varepsilon_r = 7.5$ using $\lambda/8$ discretization, showing the horn feed and lens geometry. 26

3.10 Far-field radiation patterns of discrete dielectric lenses with different discretization levels: (a) $\lambda/2$, (b) $\lambda/4$, and (c) $\lambda/8$. 27

3.11 Comparison of the far-field radiation patterns of discrete dielectric lenses with different discretization levels ($\lambda/2$, $\lambda/4$, and $\lambda/8$) at 30 GHz. 28

3.12 Simulated broadband gain response of the continuous dielectric lens across the 26–36 GHz frequency range. 29

3.13 Simulated broadband gain response of the discrete dielectric lenses across the 26–36 GHz frequency range for different discretization levels. 29
3.14 Simulated broadband gain response of the continuous and discrete dielectric lenses across the 26–36 GHz frequency range. 30
3.15 Comparison between the far-field radiation patterns of the continuous and $\lambda/8$ discrete dielectric lenses at 30 GHz. 31
3.16 Zoned lenses designed for different discretization levels using $\varepsilon_r = 7.5$, showing the horn feed and lens arrangement: (a) $\lambda/2$, (b) $\lambda/4$, and (c) $\lambda/8$. 32
3.17 Comparison of the radiation pattern of zoned lenses . 33
3.18 Simulated far-field radiation patterns across the 26–36 GHz band for zoned lenses with different discretization levels. 34
3.19 Simulated broadband gain response across the 26–36 GHz band for zoned lenses with different discretization levels. 35

4.1 Proposed UC geometry [21]. 38
4.2 Transmission magnitude (S_{21}) of chosen UC. 38
4.3 Phase response of candidate UCs across the frequency range. 39
4.4 Final TA layout constructed with the selected Unit Cells (UCs). 41
4.5 Realized gain pattern of the TA at 30 GHz. 41
4.6 Maximum realized gain of the TA in the frequency band (27–34 GHz). 42
4.7 CST model of the tilting TA used as the second lens in the Risley prism configuration. 43
4.8 CST model of the Risley prism system. The horn feed illuminates TA_1, which collimates and tilts the wavefront, while the rotation of TA_2 controls the beam steering direction. 44
4.9 Side view of the Risley prism configuration showing the relative thicknesses of TA_1 and TA_2 and the 1 mm separation between them. 44
4.10 Simulated far-field radiation patterns of the Risley prism at 29 and 30 GHz for different rotation angles of TA_2. 45
4.11 Simulated far-field radiation patterns of the Risley prism at 32 and 34 GHz for different rotation angles of TA_2. 46

List of Tables

2.1 Comparison of lens antenna types in terms of fabrication complexity, physical size, gain, and bandwidth performance. 5

3.1 Relation between the phase difference and height of the slab 22

4.1 Library of simulated UCs with corresponding geometry, transmission coefficient at 30 GHz (S_{21}), phase shift, and bandwidth (BW). 40

4.2 Comparison of the proposed TA designs with other dielectric based TAs. 47

4.3 Comparison of the proposed Risley prism configuration with other dielectric based beam steering systems. 47

List of Acronyms

MMW: Millimeter Wave

GRIN: Graded Index

AM: Additive Manufacturing

IEEE: Institute of Electrical and Electronics Engineers

EHF: Extremely High Frequency

ITU: International Telecommunications Union

RLSA: Radial Line Slot Array

PPW: Parallel-Plate Waveguide

ILA: Integrated Lens Antenna

TA: TransmitArray

UC: Unit Cell

PCB: Printed Circuit Board

FDM: Fused Deposition Modeling

3-D: Three-Dimensional

2-D: Two-Dimensional

PC: Polycarbonate

ABS: Acrylonitrile Butadiene Styrene

List of Symbols

ε_r	Relative Permittivity
ε_0	Permittivity of Free Space
ε_{eq}	Effective Permittivity
$\tan\delta_{\text{eq}}$	Effective Loss Tangent
h_{cell}	Thickness of Uniform Dielectric Slab
F	Focal Distance
ϕ_{i}	Incident Phase
ϕ_{lens}	Lens Phase
ϕ_{out}	Output Phase
ϕ_{const}	Arbitrary Phase
k_0	Free-Space Wavenumber
α_0	Main Beam Tilt
ϕ_{UC}	UC Phase
d_1	Distance between Slab Back Surface and Receiver
d_2	Distance between Slab Front Surface and Transmitter
T	Total Distance between Receiver and Transmitter
h	Slab Thickness and UC height
ϕ_{slab}	Slab Phase
$\Delta\phi$	Phase Difference between Path with Slab with Height h and Path with no Slab
r	Radial Coordinate
$h_(r)$	Height of UC in Radial Coordinate (r)
t	UC Air Inclusions Height
W	UC Air Inclusions Width
P	UC Width
S_{21}	Transmission Coefficient

CHAPTER 1

Introduction

1.1. Motivation and Context

Additive Manufacturing (AM), known as Three-Dimensional (3-D) printing, is boosting the manufacturing industry and is expected to accelerate and change engineering processes in all areas, from mechanics to biomedicine. Unlike the usual subtraction techniques, such as CNC milling, AM involves the deposition of material layer by layer. It's a faster process, uses less raw material, produces almost no waste, is cost-effective and environmentally friendly. AM is beginning to reach the field of electronics and telecommunications, which in turn supports countless areas, including the life sciences. AM is not just an alternative technology for manufacturing antennas, it opens up new challenges and previously impossible design opportunities at very low cost. This project aims to explore this technology using high permittivity materials that have recently appeared on the market to meet the need to develop cost-effective millimeter wave antennas.

The use of the K-band (20-40 GHz) for 5G communications and satellite communications can increase the capacity of these systems. The development of mobile terminals is one of the main challenges. These terminals must be compact, low cost and suitable for mass production. In addition to these characteristics, these terminals must also have high gain antennas.

The motivation behind this dissertation stems from the growing demand for advanced communication systems that require compact, efficient, and high-performance antennas. As the world moves towards higher frequency bands to meet high throughputs demand, such as the Ka-band (26-40 GHz), for satellite communications and 5G applications, the need for high-gain antennas becomes a necessity. These antennas must be capable of maintaining reliable connections over long distances. The development of 3-D-printed lens antennas using high permittivity materials offers a promising solution to meet these demands, providing a balance between performance, cost, and manufacturability.

This dissertation is part of a project that entails the development of an Lens antenna made of high permittivity materials that can be 3-D printed. By using high permittivity materials, it is possible to reduce the thickness of the Lens, thus, being easier to integrate in various applications. However, the use of high permittivity materials requires specific design processes to overcome the lens reflections.

1.2. Objectives

The main goal of this dissertation is the development of a MMW high permittivity TA antenna operating in the Ka-band using low cost AM.

The specific objectives of this dissertation are:

- Develop of a specific design procedure for TAs with high permittivity materials.
- Comparison of the high permittivity TA solutions with low permittivity materials.
- Developing a set of high permittivity unit cells to build a fully dielectric metamaterial lens compatible with AM.
- Implementation of two broadband TA antennas with high permittivity materials for a Risley Prism configuration with beam steering.

This dissertation also tries to answer these questions:

- What low cost high permittivity materials are available in the market and can be effective for the design of metasurfaces based on AM?
- Is it possible to design a compact metamaterial broadband TA antenna using high permittivity materials?

1.3. Dissertation Structure

This dissertation is organized into five chapters. The first chapter introduces the topics that are going to be talked throughout this work, outlying the motivation, objectives and main contribuitions.

The second chapter provides review of the state of the art in MMW antennas and adjacent technologies such as AM. This provides support for the work develop in later chapters. The next chapter establishes a relation between UCs and a simple dielectric slab, developing into various lens designs, the continuous lens, discrete lens and zoned lens, comparing them.

The fourth chapter presents the proposed TAs antennas. A single TA was designed and simulated as well as a risley prism configuration with two TAs both designed with a library of UCs introduced in the beginning of the chapter.

The final chapter, concludes the work done in this dissertation highlighting the manufacturability of these designs whilst using high permittivity materials that reduce the overall thickness of the lenses. It is also presented several future work developments that can be made to enhance this research topic.

1.4. Contributions

This dissertation shows that using high permittivity materials avalible comercially it is possible to design thinner TA for MMW applications, such as satellite ground segment, 5G. This also enables a versatile design for different permittivity values. Contributions for the IT group is high permittivity dilectric 3-D printed for fast and efficient TA antenna development and prototyping.

CHAPTER 2

State of the Art

2.1. Millimeter Wave Antennas

MMWs also defined as frequency spectrums in which free-space wavelengths can be described using millimeter units. These spectrums are known as Extremely High Frequency (EHF) by the International Telecommunications Union (ITU), which refers to the frequency range of 30 to 300 GHz [1].

In the last decade there has been a tremendous growth in the desire for MMW and wireless microwave communications [2]. The MMW frequency bands have proven to be of interest for a plethora of modern in-door and out-door applications [3] namely, cellular services, radar systems, radio astronomy, satellite communications, imaging applications, among others [2], [3], [4]. The previous mentioned broadband wireless communications systems, will require additional bandwidth to meet the growing demand for higher data rates [5]. However, due to higher atmospheric attenuation and absorption, and free-space path loss, MMW communication systems have limited range. Free-Space path loss, is the reduction of signal strength that depends on the distance between two isotropic antennas and the frequency at which they operate [1]. This disadvantage, has driven the research to develop efficient and high-gain antennas [6].

The Institute of Electrical and Electronics Engineers (IEEE) defines an antenna as "a mean for radiating or receiving radio waves" [7]. Better put, an antenna is the transitional structure between a guiding device and free space. The guiding device or transmission line can be a coaxial line or a hollow pipe (waveguide), that is used to transport electromagnetic energy from the transmitting source to the antenna, this is called a transmitting antenna, or from the antenna to the receiver, this is a receiving antenna [8]. A transmitting antenna connected to a transmitter, forces electromagnetic waves into free space, which then travels through space at the speed of light. Similarly, a receiving antenna connected to a receiver intercepts a portion of the electromagnetic waves traveling through space [7]. Among the most important characteristics of an antenna is its directivity,this is its ability to receive power from a specific direction or concentrate radiated power in a specific direction [9]. Another important characteristics that describes the performance of an antenna is its gain. Even though the gain of an antenna is closely related to the directivity, it is a measure that takes into consideration the efficiency of the antenna, in addition to its directional capabilities. The Gain of an antenna is defined as "the ratio of the intensity, in a given direction, to the radiation intensity that would be obtained if the power accepted by the antenna were radiated isotropically" [8]. In addition to directivity and gain another important characteristic of an antenna is its bandwidth. The bandwidth

of an antennas is defined as "the range of frequencies within which the performnace of the antenna, conforms to a specific standard" [8].

Antennas operating in the MMW spectrum must achieve high gain and efficiency to compensate for increased free-space path loss and atmospheric attenuation. Conventional antenna types, face challenges in maintaining compactness, manufacturability, and wide bandwidth at these frequencies. These limitations have motivated the exploration of alternative high-gain solutions, including dielectric and metasurface based lens antennas, which are going to be introduced in the following sections.

2.2. Lens Antennas

In these higher frequency bands, Lens antennas have emerged has a promising solution owing to their high gain, which helps mitigating propagation losses commonly encountered in these bands. Lens antennas offer advantages over alternative topologies namely antennas arrays, for instance they do not require complex feeding networks, enabling high gains at low cost [10]. A plethora of solutions have been proposed in literature, such as: dielectric lenses, geodesic lenses, dielectric Graded Index (GRIN) lens antennas [10]. Lens antennas fundamental principle is to collimate a spherical wavefront, normally generated by a feed such as a horn antenna, into a plane wave. By doing this, the energy is concentrated into a narrow directive beam, resulting in a higher gain [3], [4]. Lens antennas can also focus the recieved wavefront. One of the advantages of lens antennas lies in their simplicity when compared to phased arrays. Phase arrays achieve beamforming by using many radiating elements, each connected to an electronically controlled phase shifter. A phase shifter is a device that adjusts the phase of the signal received or radiated at each element. This allows the array to control the overall direction of the beam, enabling dynamic beam steering and multi beam operation, which provides great flexibility. However, this comes at the cost of increased complexity, high power consumption, and expensive RF hardware [1], [11]. Lens antennas, by contrast, achieve beam collimation passively through their geometry and dielectric properties, without the need for active components. While not as flexible as phased arrays, lens antennas are lighter, low power consumption and have high gain at low cost, which makes them attractive for wireless and satellite communications, imaging systems, and radar systems [10], [12].

Several lens antenna configurations have been developed, each distinguished by its operating principle, material composition, and geometrical implementation. Despite these structural and functional differences, their fundamental objectives remain the same which is to transform the spherical wave radiated by a feed into a collimated planar wavefront or focusing the radiated wavefront. Depending on the chosen approach, the lens may employ refraction through a dielectric material, along metallic surfaces, or phase control via engineered unit cells. Table 2.1 gives a overview of the principal lens antenna types.

TABLE 2.1. Comparison of lens antenna types in terms of fabrication complexity, physical size, gain, and bandwidth performance.

Antenna Type	**Ease of Fabrication**	**Size**	**Gain**	**Bandwidth**
Dielectric Lens	Feasible	Large	High	Moderate
Geodesic Lens	Moderate	Moderate	High	Large
Shaped Lens	Moderate	Large	High	Moderate
Transmitarray	Feasible	Small	High	Moderate

In Table 2.1, the different types of lens antennas are compared in complexity, performance, and implementation. Conventional dielectric and shaped lenses rely on bulk dielectric materials and curved geometries to achieve beam collimation, resulting in high gain but comparatively large structures. Geodesic lenses, on the other hand, replace dielectric refraction with metallic surfaces, significantly reducing dielectric losses and enabling wider bandwidths. TA antennas represent a recent evolution in this types of antennas, offering planar, lightweight designs through the use of engineered UCs that replicate lens phase transformation in transmission. TAs combine the high gain of conventional lenses with the design flexibility and compactness which are critical MMW and 5G applications.

Among these options, dielectric lenses stand out as one of the most used solutions, due to their simplicity and effectiveness at millimeter-wave frequencies. The following subsection discusses their main categories, design principles and applications.

2.2.1. Material Permittivity in Lens Antennas

The electromagnetic behavior of a lens antenna is strongly influenced by the relative permittivity (ε_r) of the material from which it is made. Permittivity is the dielectric property that describes how eletromagnetic waves are influenced by the material, normally observed as reflections and attenuation [13]. In free space, the permittivity is denoted by ε_0, while in dielectric materials, the relative permittivity, $\varepsilon_r = \varepsilon/\varepsilon_0$ quantifies the ratio between the two.

Permittivity controls the phase velocity of electromagnetic waves inside the lens antennas that follows to the relation $v = c/\sqrt{\varepsilon_r}$, where c is the speed of light in free space. Thus, by selecting materials with different ε_r, it is possible to control the phase delay of waves within the structure. This property is the basis of refractive lens designs, such as conventional dielectric lenses and GRIN lenses.

High-permittivity materials enable more compact lenses since a higher refractive index ($n = \sqrt{\varepsilon_r}$) allows the same phase delay to occur over a shorter physical distance. However, increasing ε_r also raises the impedance mismatch at the air–dielectric interface, leading to reflections and reduced transmission efficiency, to mitigate these effects, matching layers are often used.

The influence of permittivity on wave propagation is the foundation for dielectric lens design. In the next subsection dielectric lens antennas are presented.

2.2.2. Dielectric Lens Antennas

Dielectric lenses increase antenna directivity by transforming the spherical wave emitted by a feed at a focal point into a planar wavefront at the output aperture [6], [14]. This process enhances gain and improves collimation, making dielectric lenses one of the earliest and most widely adopted approaches for high frequency antenna systems [3]. Dielectric Lens antennas can be divided into two main categories based on the material composition they are made of.

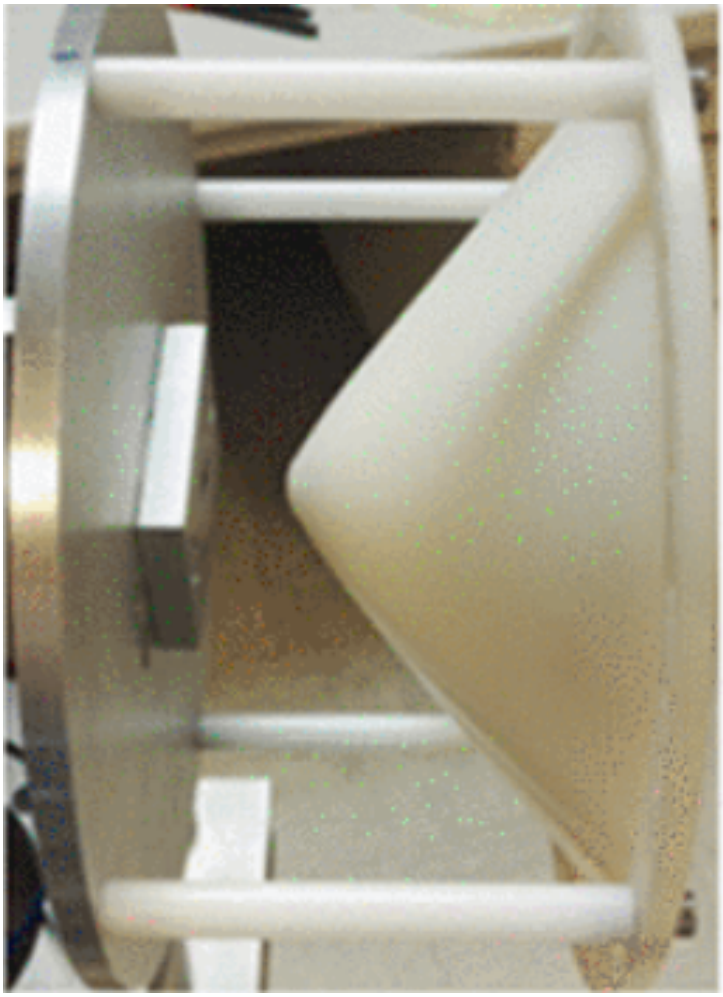
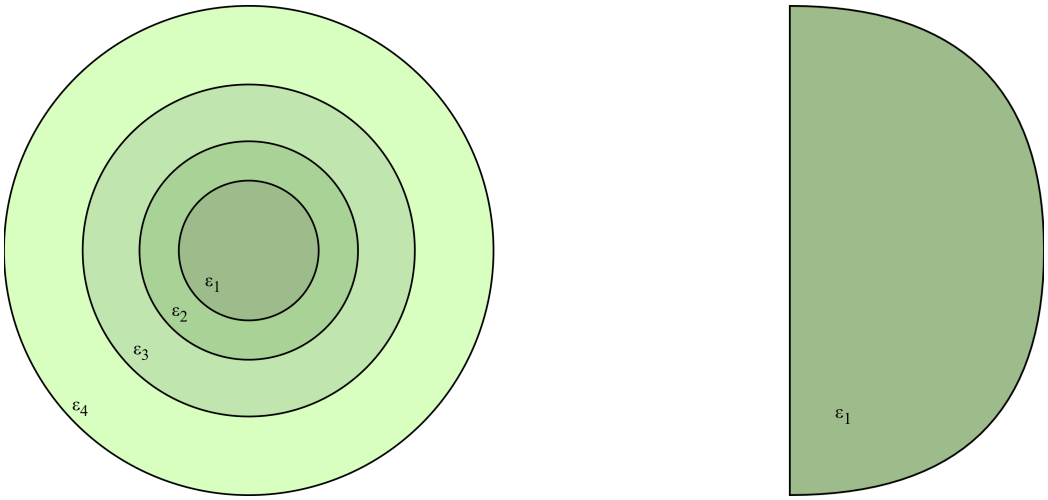


FIGURE 2.1. Example of a dielectric lens antenna [15].

The first are homogeneous lenses, which use a uniform dielectric material and achieve focusing or collimation through their curved geometry, typically designed using Snell's law. Common examples include the hyperbolic and elliptical lenses, whose surfaces are shaped so that all rays from the feed arrive at the aperture with equal phase [3], [4], [11].

The second category includes inhomogeneous, in which GRIN lenses are included. In these lenses the dielectric constant varies spatially within the structure [2], [4]. By controlling the permittivity distribution, ray trajectories can be bent. One of the most well-known examples is the Luneburg lens, which has a radially varying permittivity that allows it to focus radiation from any direction on its surface to a diametrically opposite

point. This property makes it especially useful for wide-angle scanning applications [4]. Other GRIN lens include Maxwell fish-eye [4], which are designed for specific focusing and imaging behaviors.



(A) Inhomogeneous lens (top view of a cylindrical Luneburg lens where the inner regions have higher permittivity values).

(B) Homogeneous lens (cross-section of a dielectric lens with a uniform ε_r corresponding to the lens material).

FIGURE 2.2. Examples of dielectric lens classes: (a) Inhomogeneous and (b) Homogeneous.

Figure 2.2 illustrates the difference between homogeneous and GRIN dielectric lenses. In the homogeneous case, refraction occurs entirely due to the curved surface profile, whereas in the GRIN case, the gradual permittivity variation bends rays internally, allowing for flatter external surfaces. Another variant of the Dielectric Lenses are the zoned lenses, which reduce the bulk of conventional dielectric lenses. These lenses segment the continuous curved profile into concentric zones that maintain the same desired phase transformations but with reduced thickness. This makes them lighter and less lossy, though the stepped transitions can introduce shadow losses [16], [4], [17]. Shadow losses or shadow blockage effect, decreases the gain on these antennas [16]. An alternative approach to achieve a thinner profile than the conventional dielectric lenses is found in GRIN lenses. Rather than physically shaping or zoning the dielectric, GRIN lenses rely on a gradual variation of permittivity within the material to bend rays along desired trajectories. GRIN lenses, have the same role as conventional dielectric lenses of collimating spherical waves from a feed into a plane wave, thus producing a highly directive beam and beamsteering. The key difference is that instead of using surface curvature, a GRIN lens can be fabricated with a flat profile, where the refractive index varies locally to manipulate ray paths [14]. Despite their effectiveness, dielectric lenses face challenges such as bulkiness at MMW frequencies [18], partial reflections due to impedance mismatch at the air dielectric interface [19], and potential fabrication difficulties when complex geometries are required. Despite these limitations, dielectric lenses are widely used because they combine simplicity, low cost, and high gain in a single solution [4], [11].

2.2.3. Geodesic Lenses

Unlike dielectric lenses, which rely on material permittivity and lenses curvarture to bend and collimate electromagnetic waves, geodesic lenses achieve the same effect through the geometry of a conducting surface. In geodesic lenses, rays are guided along designed curved metallic materials, where the path length differences replicate the collimation normally achieved by refraction. This makes geodesic lenses attractive for high-frequency systems, as they can reduce material losses while still offering the directive properties of conventional lenses [11]. An example of a fabricated geodesic lens in [20] is shown in Fig. 2.3.



FIGURE 2.3. Illustration of a geodesic lens concept. The curved metallic surface guides electromagnetic waves along paths equivalent to those in a graded-index dielectric lens [20].

This type of lenses received the attention of the antenna community due to their low cost and high efficiency. Geodesic lenses use the physical path that mimics an equivalent graded refractive index. These lenses can be implemented in a fully metallic configuration using parallel plate waveguides, which differs from conventional lenses. This makes them ideal for high frequency applications, where dielectric materials have prohibitive losses. Geodesic lenses can also mimic the properties of GRIN lenses, that provide wide-angle scanning capabilities with reduced scan losses. [20]. While geodesic lenses address some of the loss and bulk issues inherent to the dielectric approaches, another type of high gain antenna is the TA antenna. Unlike conventional lenses or reflectors, TAs use an array of engineered UCs across a planar surface to impose precise phase shifts on the passing wavefront, effectively shaping the outgoing beam [21], [22]. In the next section, it will be presented the TA antennas, exploring their operating principles, advantages, and challenges.

2.2.4. TransmitArrays

TA play a significant role in millimeter-wave communications due to their simple structure, ease of fabrication, and design flexibility. A TA operates as a lens, it shapes the phase of the incoming electromagnetic wave radiated by the feed so that the transmitted wavefront forms a highly directive beam [21]. Unlike conventional dielectric lenses, which rely on bulk material curvature or refractive index gradients to bend rays, TAs achieve the same effect through refraction. Each UC of the array applies a phase delay to the incident wave, effectively sampling the required aperture distribution and reconstructing the desired wavefront in transmission. This makes TA function like a Fresnel lens [21]. TAs can be referred to as a metasurface, since they are composed of engineered UCs which provides a far greater flexibility compared to conventional dielectric lenses [21]. Metasurfaces are planar, subwavelength-engineered structures capable of locally controlling the phase, amplitude, and polarization of electromagnetic waves [23]. A TA can be regarded as a metasurface lens, where the collective response of its UCs performs the same wavefront transformation as a conventional lens but within a thin profile. A more detailed discussion on metasurfaces is done in Section 2.4.

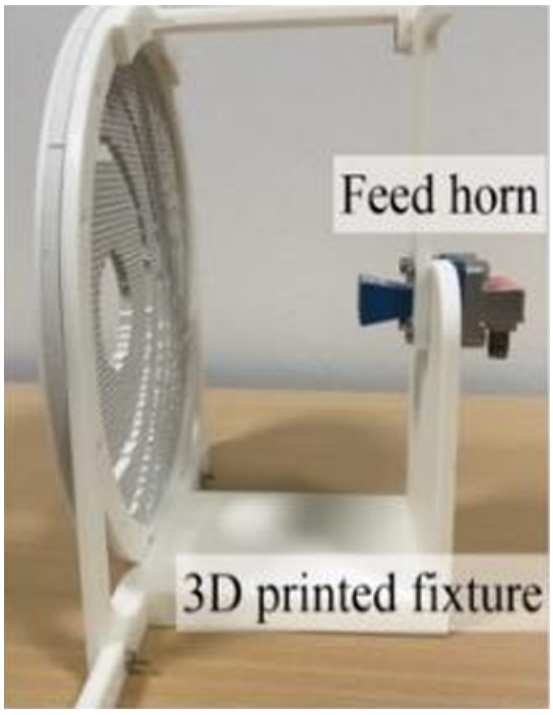


FIGURE 2.4. Example of a TA, with a 3-D printed stand for the Lens and the feed horn [21].

A major strength of TAs lies in their design versatility. By adjusting cell geometry, material, it is possible to achieve the desired phase shift and transmission characteristics [21]. Ensuring that the UC periodicity remains below half the wavelength prevents grating lobes [8], allowing a discretized TA to approximate a continuous lens profile, thus a more accurate local phase shift.

There is also an approach were the TA employs PCB based UCs, consisting of a multilayer stack with patterned metal layers, referred to as PCB TA. Compared to reflectarrays, which use similar phase-engineered cells but operate in reflection, TAs avoid feed blockage and often achieve higher aperture efficiency [22]. Their transmission based nature makes them particularly attractive for satellite links, backhaul communications, and radar systems where compactness and efficiency are key.

Another application of TAs is the introduction of beam steering capabilities using passive structures. A possible approach is inspired by the Risley prism, which achieves beam deflection through the relative rotation of two prisms or two dielectric wedges [24]. In a microwave domain implementation, this concept can be realized by cascading two TAs, each providing a phase gradient across the aperture. By rotating one TA with respect to the other, the combined phase response results in a controllable steering of the radiated beam. This configuration enables continuous beam steering without the need for active components, phase shifters, or complex feeding networks.

Nevertheless, TAs also face challenges. Optimizing both transmission amplitude and phase simultaneously is non-trivial, especially when high permittivity dielectrics are involved, since impedance mismatch and resonances can degrade performance [2], [6], [25].

Despite these challenges, transmitarray antennas represent a natural evolution in lens antennas: combining the gain and focusing ability of classical dielectric lenses with the flexibility of modern engineered metasurfaces.

2.3. Feeds for Lens Antennas

There are different types of lens antennas feeding methods, where horns, microstrip, dipoles and arrays of antenna elements are normally used [11].

Lens antennas require a feed to illuminate the aperture with an wavefront. The choice of the feed has a direct impact on efficiency, sidelobe levels and beam performance, since it determines how well the aperture of the lens is illuminated. Feeds can be distinguished by how they interact with the lens and by their position relative to it. Based on this, they can be separated into three classes, spatial feeds, leaky-wave feeds, and integrated feeds.

2.3.1. Spatial Feeds

Spatial feeds are characterized by the existence of a focal distance between the feed and the lens aperture. In this configuration, the feed radiates a spherical wavefront into free space, and the lens transforms this wave into a collimated or focused beam. The performance of a spatially fed lens antenna depends strongly on the feed's radiation pattern, since it determines how well the aperture is illuminated. A narrow beam can under-illuminate the lens, wasting effective aperture area, while an overly wide beam produces spillover losses and reduces overall efficiency [8]. Common examples of spatial feeds include horn and microstrip (patch) antennas.

The horn antenna is one of the simplest and most widely used types of spatial feeds [8]. The horn is a simple radiator excited by a wave guide, being its natural extension

[9]. In addition to its function as a focal point feed for lenses and reflectors, it is a common element of phased arrays and serves as a universal standard for calibration and gain measurements of other high gain antennas [8], [9]. This antenna is utilized as a feed element for large satellite tracking, radio astronomy and communication dishes installed around the globe [8].

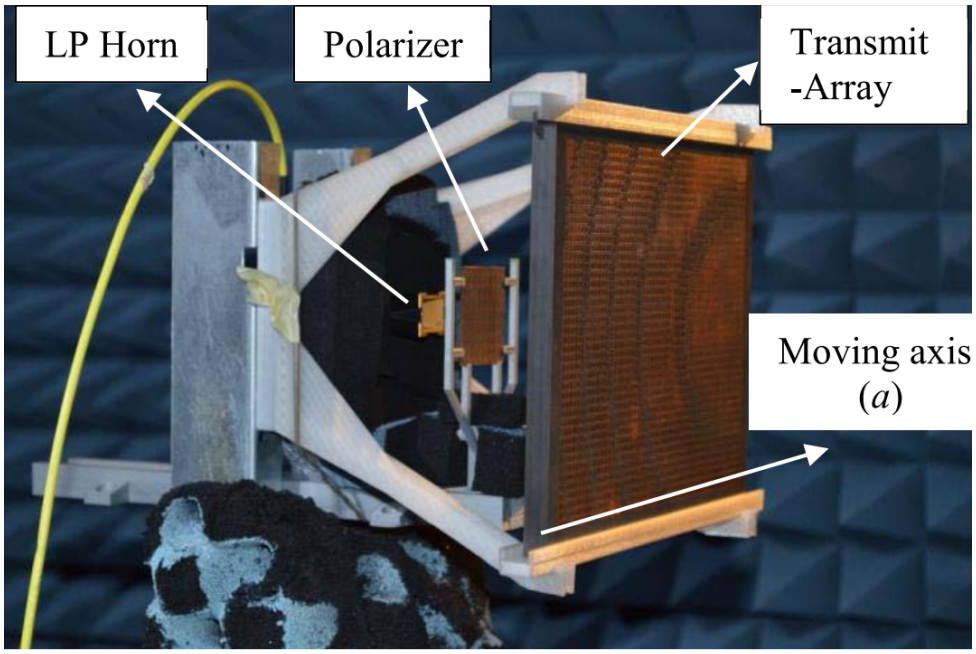


FIGURE 2.5. Illustration of a spatial-feed antenna system, taken from [26]

The microstrip or "patch" antenna represents another form of spatial feed. They consist of a metal patch suspended over a ground plane with a dielectric material between them [7]. Microstrip antennas are typically used in applications such as, satellite, aircraft, spacecraft and missile applications, where weight, size, cost, performance, aerodynamics profile and ease of installation are restrictions. These antennas are low profile, mechanically robust when installed on rigid surfaces, conformable to planar and non planar surfaces, simple and cheap to manufacture using modern printed-circuit technology. Major disadvantages of these antennas are their low gain, narrow bandwidth, low power, low efficiency, poor polarization and low scan performance [7], [8].

Overall, spatial feeds remain one of the most widely used approaches for lens illumination due to their simplicity and performance. However, their physical separation from the lens can restrict integration in certain applications, where a large focal distance is not feasible. This limitation can be addressed through leaky-wave or integrated feeding architectures, discussed in the following subsections.

2.3.2. Leaky Wave Feeds

Leaky-wave feeds do not rely on a discrete focal point. Instead, they radiate continuously along their guiding structure, coupling a portion of the guided energy into free space as the wave propagates. According to [8], a leaky-wave antenna is “an antenna that

couples power in small increments per unit length, either continuously or discretely, from a traveling-wave structure to free space." Because energy is gradually radiated rather than emitted from a single point, the fields decay along the direction of propagation and increase in the radiation direction, producing a directive beam [8].

This allows leaky-wave feeds to generate an effective phase front that can emulate the illumination produced by a focal source, but without requiring large spatial separation between the feed and the lens. Consequently, leaky-wave feeds are attractive for compact and planar lens configurations, where minimizing the focal distance important.

The leaky-wave antenna can also be implemented using a Radial Line Slot Array (RLSA) structure, which operates by exciting a guided wave that gradually leaks energy through an array of radiating slots. An RLSA consists of a Parallel-Plate Waveguide (PPW), in which a radially propagating mode is excited to feed a slot distribution etched on the upper metallic plate of the PPW [27].

Figure 2.6 shows a fabricated RLSA prototype. The structure consists of a circular metallic plate patterned with precisely arranged slots that follow a spiral distribution, designed to control the phase of the leaking wave.

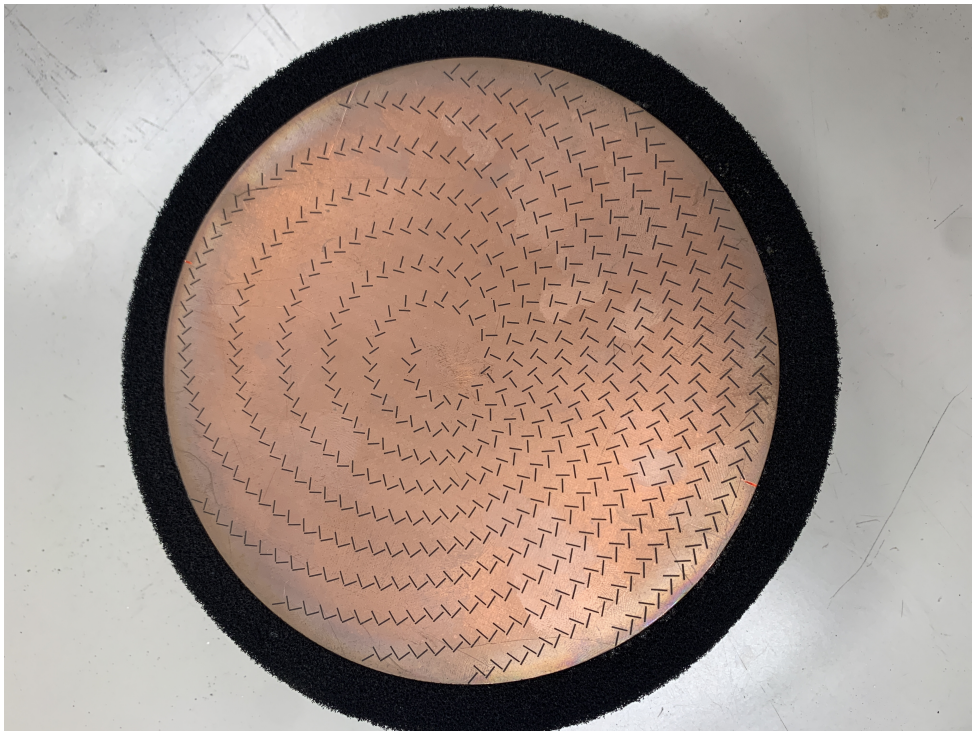


FIGURE 2.6. Fabricated RLSA antenna used for leaky-wave radiation studies, taken from [28].

Overall, leaky-wave feeds offer a promising compromise between the simplicity of spatial feeds and the integration potential of fully embedded architectures. Their continuous-radiation nature makes them especially suitable for low profile and beam scanning MMW lens antennas, where compactness and mechanical simplicity are critical.

2.3.3. Integrated Feeds

Integrated feeds embed the radiating element within the lens structure itself. In this configuration, the physical separation between the feed and the lens aperture is eliminated, allowing the feed to become part of the system. This integration enables compact, mechanically robust antenna architectures, where the radiating aperture is either printed with the lens body or coupled directly through embedded waveguides within the dielectric material.

Integrated Lens Antennas (ILAs) are characterized by having the feed in direct contact with the lens body, within it, or at a sub-wavelength distance from it [4]. Figure 2.7 shows a example of a integrated feed.



FIGURE 2.7. Example of an integrated feed antenna system, taken from [4] "ILA fed by a planar self-complementary log-periodic feed".

In summary, integrated feed configurations offer an effective way to reduce the overall antenna system size by directly coupling the feed and the lens structure. These architectures enable more compact antenna systems. Unlike conventional dielectric lenses, metasurfaces manipulate electromagnetic waves through subwavelength elements, enabling flat and lightweight alternatives for wavefront control. In the following section, metasurfaces are going to be discussed.

2.4. Metasurfaces

Metasurfaces are planar structures or two-dimensional version of metamaterials. These structures can locally modify the phase, polarization and amplitude of light in reflection or transmission. This enables the production of patterned flat optical components, where

it is possible to control their functionality by design [23]. These structures mitigate undiserable losses and dispersions in wave propagation, being also suitable for a easy micro and nano-structues fabrication [29].

Metamaterials are artificially designed 3-dimensional periodic structures synthesized to produce materials with customisable and unique properties that cannot be exhibited by natural occurring materials. [30], [29].

They are artificial eletromagnetic media that consist of periodic sub-wavelength metal or dielectric structures at a smaller scale than their operating wavelengths [23]. There are numerous types of metamaterials, namely, eletromagnetic, Piezoelectric, terahertz, acoustics, absorbers, non-linear metamaterials and frequency selective surface based metamaterials [23], [31].

A plethora of applications is available due to matematerials unique properties, such as, general safety, sensor identification, improved ultrasonic sensors, high frequency battle field communications, solar energy management for high gain antennas, metamaterial enhanced magnetic induction and remote aerospace [23], [32].

Another application of metamaterials is the transformation of wavefront electromagnetic waves. Electromagnetic waves propagate perpendicularly to the phase fronts in free space, where it is feasible to change the wavefront of the wave momentarily [25].

These materials have the ability to create highly directive radiation beams from simple sources namely dipoles or slots inside them [33].

The surfacing of AM has transformed the set of tools available to metamaterials researchers. It is now possible to exert control over multiple length scales within single-step processes and leverage entirely new geometrical and material design freedoms [32].

2.5. Additive Manufacturing

Additive manufactoring is a technology that discretizes a 3-D model into a Two-Dimensional (2-D) plane, shapes the 2-D plane from points to lines, and manufactures it layer-by-layer into the 3-D part. It employs a computer design technology to create the 3-D objects, which are then sent to the printer [34].

AM offers several advantages over conventional manufacturing, including the efficient use of materials and resources, flexibility in production and part design. However, AM has its drawbacks such as, size limitations, surface imperfections and high equipment costs. Despite these challenges, AM enables quick prototyping, reduced design errors and allows a faster market entry for designed products.

There are different AM techniques and processes. Some processes use thermal energy from laser or electron beams, which is directed via optics to melt or sinter (form of a coherent mass without melting) metal or plastic powder together. There are also processes that use inkjet-type printing heads to accurately spray binder or solvent onto powdered ceramic or polymer. Examples of Fused Deposition Modeling (FDM) techniques are FDM, Laminated Object Manufactoring, Laser engineered net shaping, Stereo lithography, Selective laser sintering.

FDM is a 3-D printing process in which a thin layer of thermo plastic wire filament is extruded from a print head, where it is heated to around 2^{o}C above of its melting point The filament solidifies almost immediately after extrusion, bonding with the previous layers. Materials used in FDM are Polycarbonate (PC) and Acrylonitrile Butadiene Styrene (ABS) [35].

The principles of design methodology of dielectric TAs is presented in the next chapter.

CHAPTER 3

Design Methodology of Dielectric TA

The purpose of this chapter is to establish a theoretical and numerical foundation for understanding how high permittivity dielectric materials can be used to control the phase response in MMW lens antennas. Rather than beginning immediately with complex discretized UC geometries, a simplified model was first analyzed, a single dielectric slab of variable height. This preliminary step allows the study of the relationship between slab thickness, material permittivity, and the resulting phase delay, which is the key mechanism later used in the UC design. In addition to these preliminary simulations, this chapter also introduces the dielectric material that will be used throughout the rest of this dissertation. The selection of the material is motivated both by its electromagnetic properties (high permittivity) and by its compatibility with AM techniques, ensuring that the designs studied here can be implemented. The analysis was carried out both theoretically and through full-wave simulations in CST Microwave Studio, providing a comparison between theorical equations and realistic results that include reflections, transmission effects, and the influence of material interfaces. This chapter concludes with a comparison between continuous and discretized lens models, followed by the introduction of a zoned lens design. These simulations extend the UC and slab analysis into more complex structures, that will lead to the design of the TA in Chapter 4.

3.1. UC and TA Design

As mentioned in the last chapter, the operating principle of a lens antenna is to transform a spherical wave into a planar or collimated wavefront. This transformation is achieved by controlling the phase distribution across the aperture so that all rays coming from the lens have the same phase regardless of their path. In conventional dielectric lenses, this phase control is obtained through the physical curvature of the dielectric surface or by locally varying the material permittivity, which can be achieved by changing the material itself or by tunning the infill of the material. In discrete or TA lenses, however, this same principle can be implemented using UCs. Each UC acts as an individual phase-shifting element that modifies the phase of the transmitted wave according to its geometry and material. When periodically arranged across the aperture, the response of all UCs reproduces the desired phase profile, enabling the formation of a highly directive beam. This is the principle in which the lenses presented in this chapter are based on. The study of UCs is crucial for understanding how dielectric thickness and geometry can be used to control phase delay at MMW frequencies. This section presents a overall study on UCs.

Analyzing a UC under periodic boundary conditions can be the same as observing a slab model when the geometry is a dielectric block of variable height. Moving to the UC framework has the advantage of being valid for any given geometry of the cell as long as the periodicity of the cell is smaller than half the operating wavelength. This design rule is used to prevent grating lobes [8]. For cells that are made of low permittivity dielectrics, even geometries that have holes or voids can still be accurately described by the slab model, approximated by an effective permittivity [21]. However, as the dielectric permittivity increases these relations do not apply equally. With higher permittivity, the impedance mismatch at the air–dielectric interface increases, stronger diffraction effects occur, and total internal reflections may appear inside the UC. These effects affect the transmission response of the UC significantly, often appearing as resonances [21].

The concept of UC can be simplified using a homogenized model. When the dielectric and air within the UC are treated as an equivalent homogeneous medium, the UC can be characterized by an effective permittivity (ε_{eq}) and an effective loss tangent ($\tan\delta_{\text{eq}}$). These parameters represent the averaged permittivity values of the materials that compose the UC. In this work, only the dielectric material and air are considered. This homogenized representation provides a simplified yet accurate way to describe the electromagnetic behavior of the UC.

When reflections at the air–dielectric interfaces are small, the model can be further simplified using the single-ray approximation. Under this assumption, the UC behaves as a uniform dielectric slab of thickness h_{cell} and effective permittivity ε_{eq}. This equivalence forms a useful bridge between the detailed UC structure and the analytical slab model discussed in the next section. Figure 3.1 illustrates this homogenization process.

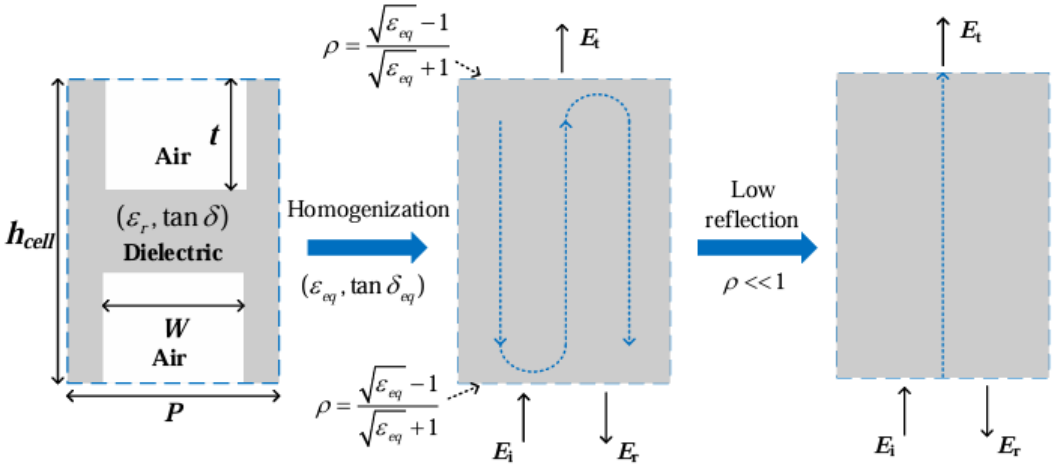


FIGURE 3.1. Homogenized representation of a dielectric UC [21].

It is now possible to contrast the UC approach with the idea of a conventional dielectric lens. Traditional dielectric lenses are bulk structures whose curved profiles are designed using Snell's law, which bends rays at the air–dielectric interface to collimate or focus radiation. These designs typically result in large structures, which are not ideal for

compact MMW systems. UCs, however, do not rely on Snell's law or curved geometries. They make use of the thin-lens approximation, where the lens is assumed to be locally perpendicular to the incident wavefront. Each cell, controlled to provide a phase delay, is arranged in the aperture, synthesizing the desired wavefront transformation [36].

UCs, as mentioned earlier, do not follow Snell's law, which describes how rays bend at dielectric interfaces based on material indices. Their role is to provide a controlled phase delay that can be assigned directly to a position on the lens aperture. Each UC is placed at coordinates (x, y) and designed to impose the phase required at that location so that the overall aperture produces the desired transformation of the wavefront.

The required aperture phase distribution can be derived by considering the propagation path from the feed to the lens and then through free space. At the input plane of the lens, the phase of the spherical wave radiated by the feed is:

$$\phi_i(x, y) = k_0\sqrt{x^2 + y^2 + F^2}, \tag{3.1}$$

where k_0 is the free-space wavenumber and F is the focal distance. Ideally, the output wavefront after the lens should be planar, meaning the total phase is constant across the aperture. This requires that the lens itself introduces a phase shift $\phi_{\text{lens}}(x, y)$ such that:

$$\phi_{\text{out}}(x, y) = \phi_i(x, y) + \phi_{\text{lens}}(x, y) = \text{constant}. \tag{3.2}$$

From this condition, the required lens phase distribution is expressed as:

$$\phi_{\text{lens}}(x, y) = -k_0\sqrt{x^2 + y^2 + F^2} + \phi_{\text{const}}, \tag{3.3}$$

where ϕ_{const} is an arbitrary reference phase that does not affect the wavefront transformation but can influence how the UC phases are wrapped around 2π during implementation, which can have positive effects on performance. A TA can be designed with an arbitrary phase profile, enabling a wider range of applications beyond simple collimation. For instance Equation 3.3 can be generalized to include an offset beam tilt, as shown below:

$$\phi_{\text{lens}}(x, y) = -k_0\sqrt{x^2 + y^2 + F^2} - k_0 x \sin(\alpha_0) + \phi_{\text{const}}, \tag{3.4}$$

where α_0 is the desired tilt angle of the main beam.

The phase profile of the TA defines the local phase of each UC. The phase required (calculated at the centre of the UC) is mapped to a specific geometry previously obtained by UC analysis. In the simple dielectric slab model, this can be achieved by changing the cell height.

For simple slab like UCs described in detail in the next section, the mapping between phase delay and height can be obtained directly from the relation:

$$\phi(h) = k_0(\sqrt{\epsilon_r} - 1)h, \tag{3.5}$$

which may be inverted to determine the height corresponding to a target phase shift. For more complex geometries, particularly when high-permittivity dielectrics are used, the phase response cannot be described by this analytical formula alone. The exact transmission phase requires full-wave simulations of the UC undder periodic boundary conditions.

The aperture can be discretized with different UC periodicities, which is going to be studied later in this chapter. The analysis of UCs establishes a relation between geometry, material properties, and phase control in fully dielectric TAs. By using the homogenized model, it becomes clear that each UC behaves as an equivalent dielectric slab whose thickness determines its phase delay. This not only simplifies the analysis but also provides a direct path toward analytical modeling through the slab analogy. In the next section, this relationship is explored in more detail by analyzing the canonical dielectric slab model, which serves as the foundation for understanding the phase response of the UC and, ultimately, of the complete lens structure.

In conclusion, the analysis of the UC establishes a relation between geometry, material properties, and phase control in a dielectric based TA. By using a homogenized model, each UC can be viewed as an equivalent dielectric block whose thickness determines the phase delay it introduces. This perspective not only simplifies the analysis but also creates a bridge to the analytical slab model. In the next section, this relationship is going to be explored, using the dielectric slab as a simplified representation to understand how thickness influences the phase response.

3.2. Slab Model

By representing the UC as a single block of dielectric material with uniform thickness, it becomes easier to study how the material and its height influence the transmitted phase. To better understand how dielectric thickness influences phase control at MMW frequencies, a simplified slab model was developed in CST Microwave Studio. The geometry is shown in Fig. 3.2.

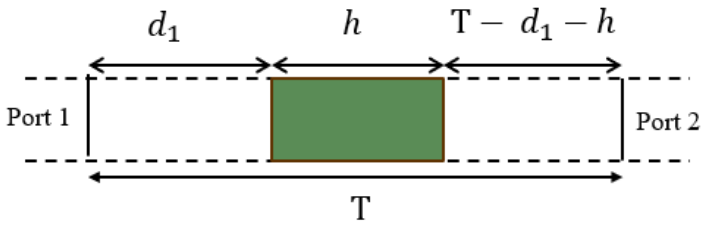


FIGURE 3.2. Single dielectric slab model with transmitter (Port 2), receiver (Port 1), and slab height h.

The model consists of a dielectric slab of thickness h placed between two wave ports. The total distance between the transmitter (Port 2) and receiver (Port 1) is denoted by T. The distance from the transmitter to the front surface of the slab is d_2, while the

distance from the slab's back surface to the receiver is d_1. It is possible to express these as:

$$d_2 = T - d_1 - h, \tag{3.6}$$

$$T = d_1 + h + d_2. \tag{3.7}$$

Electromagnetic waves propagate partly through free space and partly through the dielectric slab. The wavenumber in free space is:

$$k_0 = \frac{2\pi f}{c}, \tag{3.8}$$

where f is the frequency and c is the speed of light. The phase accumulation through the structure can be described analytically. For a dielectric slab of thickness h and relative permittivity ϵ_r, the phase contribution is:

$$\phi_{\text{slab}}(h) = k_0\sqrt{\epsilon_r}\, h. \tag{3.9}$$

The phase contribution of the air section of length $(T - h)$ is:

$$\phi_{\text{air}}(h) = k_0(T - h). \tag{3.10}$$

Thus, the total phase accumulated when the path includes a dielectric slab of height h is the sum of the contributions across the slab and the air portion:

$$\phi(h) = k_0(T - h) + k_0\sqrt{\epsilon_r}\, h. \tag{3.11}$$

The reference case (no slab, $h = 0$) has phase:

$$\phi(0) = k_0 T. \tag{3.12}$$

Therefore, the phase difference introduced by inserting the slab is:

$$\Delta\phi = \phi(h) - \phi(0) = k_0(\sqrt{\epsilon_r} - 1)h. \tag{3.13}$$

As observed in Eq. (3.13), the phase shift is directly proportional to the slab thickness and scales with the material permittivity ϵ_r. Increasing either the slab height or the permittivity increases the delay imposed on the wave.

Rearranging Eq. (3.13), for any target phase shift $\Delta\phi$, the required slab height can be written as:

$$h = \frac{\Delta\phi}{k_0(\sqrt{\epsilon_r} - 1)}. \tag{3.14}$$

This result shows the relationship between dielectric thickness and phase delay. In the simplified slab model, phase control is achieved by adjusting the height h, which changes

the optical path length experienced by the propagating wave. Using this relation, it is possible to determine the slab height required to introduce a given phase shift.

This process is known as discretization. The aperture of a lens can be divided into segments (or later, UCs), each designed to produce a specific phase delay. To illustrate this, a 2-bit discretization was performed, considering three target phase shifts of $\Delta\phi = \pi/2, \pi, 3\pi/2$. For each of these values, the corresponding slab height was calculated assuming a dielectric permittivity of $\epsilon_r = 7$ and a design frequency $f = 30\,\text{GHz}$.

TABLE 3.1. Relation between the phase difference and height of the slab

$\Delta\phi$	h
$\frac{\pi}{2}$	1.52
π	4.56
$\frac{3\pi}{2}$	3.04

Having determined the theoretical slab heights corresponding to the target phase delays, the next step was to validate these results through full-wave simulations. While the analytical expressions provide a relationship between thickness and phase shift, they do not account for secondary effects such as reflections at the air–dielectric boundaries. To assess if the theoretical predictions are supported in pratice, the three slab configurations listed in Table 3.1 were implemented in CST Microwave Studio and their phase responses were simulated. The resulting phase response is shown in Fig. 3.3.

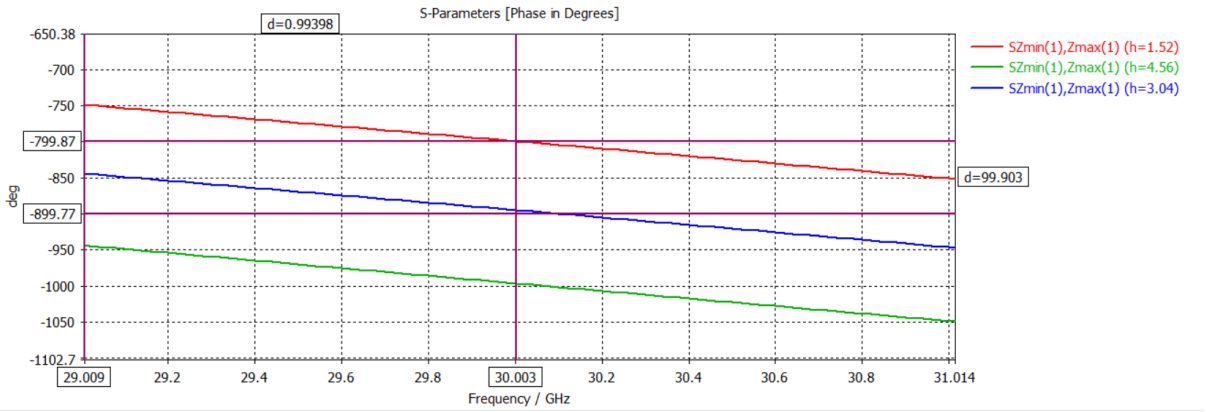


FIGURE 3.3. Simulated absolute phase response for different slab heights h.

Figure 3.3 presents the simulated phase responses of the three slab configurations at the design frequency range around 30 GHz. The results confirm the theoretical expression that increasing the slab thickness produces a corresponding increase in phase delay. For the heights calculated in Table 3.1 (1.52 mm, 3.04 mm, and 4.56 mm), the phase differences between the curves are close to the expected $\pi/2$ increments.

Although small deviations are visible, mainly as offsets in the phase values, these come from interface reflections included in CST but neglected in the analytical model.

The phase response of the slabs remains consistent with the theoretical expression, which validates the model and the expressions.

It was also simulated the amplitude response of these slabs, Figure 3.4 shows the obtained results.

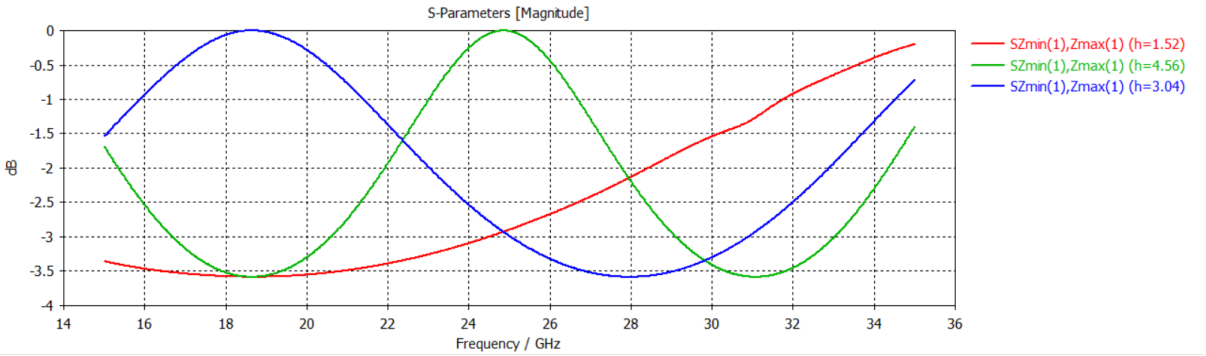


FIGURE 3.4. Simulated transmission for different slab heights h.

Figure 3.4 shows that these slabs, have low amplitude responses. This effect can be explained by the high permittivity material, which causes reflections. Thus this geometry is not optimal for later designs. The final geometry is going to be introduced in chapter 4.

The slab simulations not only confirmed the analytical expression between dielectric thickness and phase delay but also how parameter variations influence wave behavior at MMW frequencies. It became possible to see how slab height can be used to tune the phase response, while also observing secondary effects, such as reflections, that shift the results away from the theorical value. This analysis helped to understand how phase can be controlled through material thickness, which directly connects to the lens design presented in the following sections.

3.3. Lens Design with variable height UC

The slab model confirmed that dielectric thickness can be used to control phase delay in a predictable way and that these phase values can be discretized into a slab height.

In this section it will be used the previous slab UC considering a permittivity of ϵ_r=7.5 (value for the commercial dielectric material Zetamix ϵ) to design a collimated TA. A spatially fed TA antenna, with a horn as the primary source placed at the focal distnace F=100 mm. The aperture size of the lens is set to D=140 mm. For this case, it is going to be studied the effect of considering different discretization steps without zoning (to be studied in the next section). These results are compared with the refence lens design, a continuous lens where the periodicity tends to zero.

To investigate this, two approaches were considered. The first treats the lens as a continuous homogeneous dielectric structure, with its profile defined by the aperture phase distribution required for collimation. The second interprets the lens as an array of discrete UCs with uniform periodicity but variable heights, each introducing a specific phase delay. These two approaches are important in order to see how different ways of

shaping the dielectric could be used to achieve a collimated beam. The continuous design can be seen as a reference for the ideal case, while the discrete approach is a first step toward structures that are easier to build using AM. In this section, both methods are implemented and their results are compared.

The calculation of the lens profile is based on the principle that, for a focal point located at a distance F from the horn aperture, the phase delay along all paths from the horn to the output of the lens must be equal. In other words, each point on the lens must introduce a height dependent delay such that the wavefront is planar and highly directive. This leads to the following expression:

$$h(r) = \frac{1}{\sqrt{\epsilon_r} - 1} \left(F + \sqrt{\epsilon_r - 1} \cdot h_{\text{total}} - \sqrt{r^2 + F^2} \right), \tag{3.15}$$

where h_{total} is the maximum lens height, ϵ_r is the dielectric relative permittivity, which is 7.5 throughout this chapter, F is the focal distance (100 mm in this case), and r is the radial coordinate on the lens aperture. This formula defines the lens thickness required at each position to ensure that all transmitted rays emerge in phase, forming a directive beam.

Using this relation, a continuous lens was designed and implemented in CST Microwave Studio. The model included both the feed horn and the dielectric lens with a relation F/D = 0.7, with the lens profile shaped according to Equation 3.15 with a thickness of $2.6\lambda_0$. The resulting geometry is illustrated in Figure 3.5.

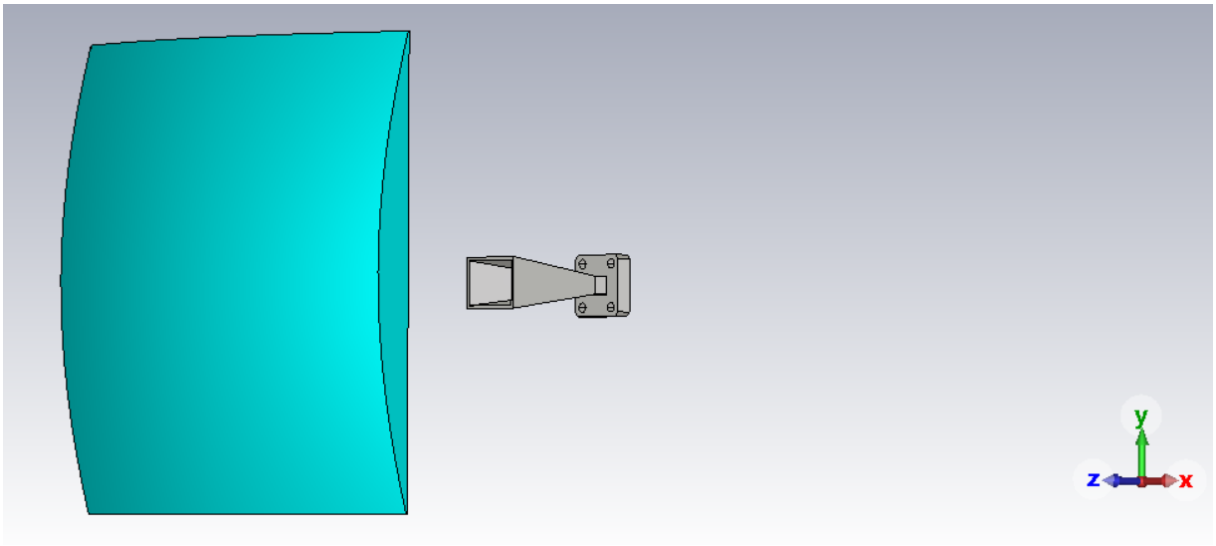


FIGURE 3.5. Continuous lens model implemented in CST.

Once the continuous lens model was defined in CST, its far-field was simulated at the design frequency of 30 GHz. The resulting radiation pattern is shown in Figure 3.6. The lens successfully transforms the spherical wavefront of the horn into a narrow directive beam, as the main lobe is centered at 0°. The peak realized gain reaches 29.3 dBi with a 3 dB beamwidth of 4.6°. The sidelobe level is −20.5 dB.

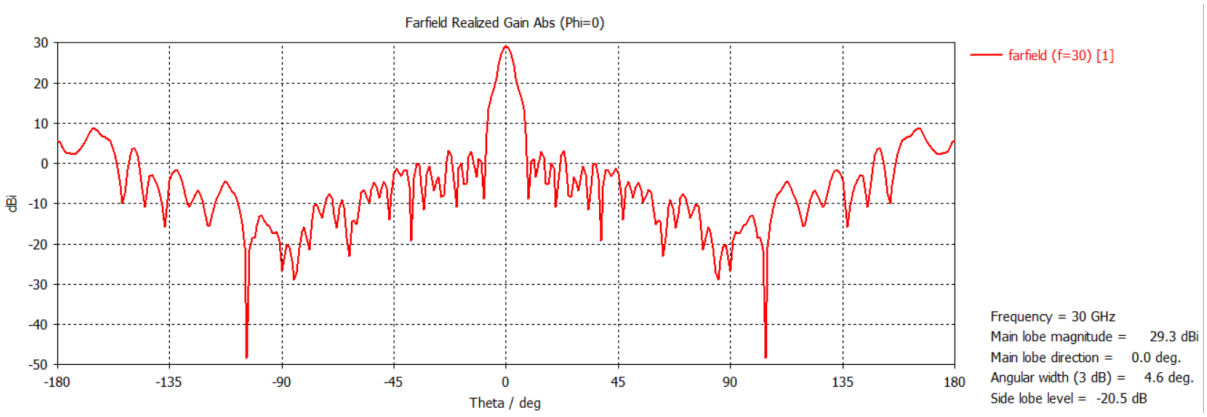


FIGURE 3.6. Radiation pattern of the continuous lens.

While the continuous lens provides a useful reference and demonstrates the theoretical phase profile required for collimation, its geometry is not practical to manufacture with dielectric materials or additive fabrication methods. To address this, the second approach interprets the lens as a discrete array of UCs, with uniform periodicity but with a height chosen to impose the required phase delay. Before analyzing the discrete lens, it is important to introduce the concept of discretization.

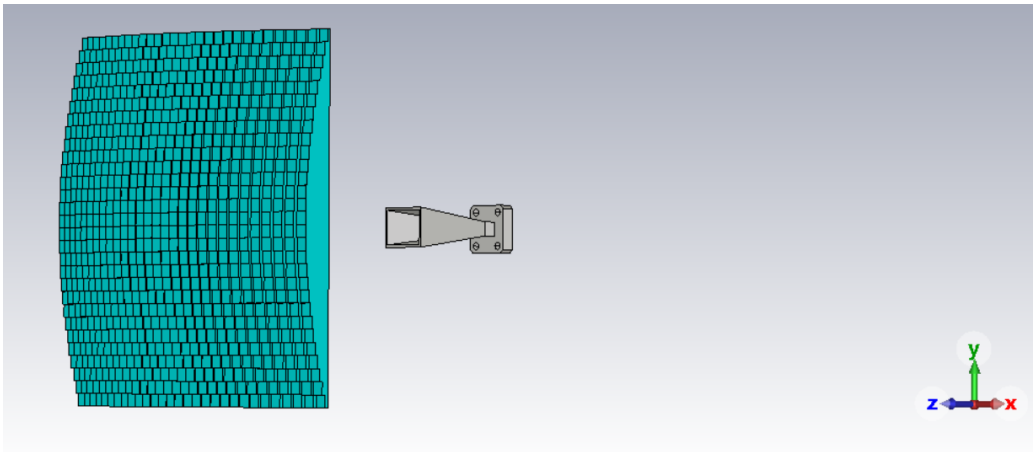


FIGURE 3.7. Discrete lens designed with $\varepsilon_r = 7.5$ using $\lambda/2$ discretization, showing the horn feed and lens geometry.

In practice, when the continuous lens profile is translated into a structure composed of individual UCs, the smooth phase variation across the aperture must be sampled at discrete intervals. Each of these intervals corresponds to one UC, whose size is defined by the periodicity, which is determined by the discretization level. To avoid grating lobes, the periodicity is typically chosen to be smaller than or equal to half the wavelength ($\lambda/2$). The discretization level defines how finely the continuous phase profile is represented: a smaller periodicity (that is, a higher discretization level) provides a closer approximation to the ideal continuous phase distribution, while a larger periodicity simplifies fabrication but introduces coarser phase steps.

The discrete lens models shown in Figures 3.7, 3.8, and 3.9 were designed based on this principle, using three different discretization levels $\lambda/2$, $\lambda/4$, and $\lambda/8$.

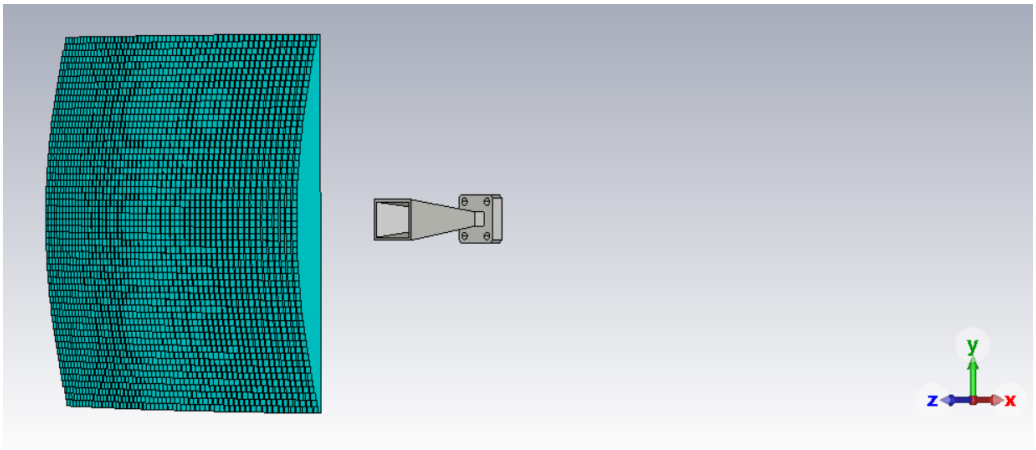


FIGURE 3.8. Discrete lens designed with $\varepsilon_r = 7.5$ using $\lambda/4$ discretization, showing the horn feed and lens geometry.

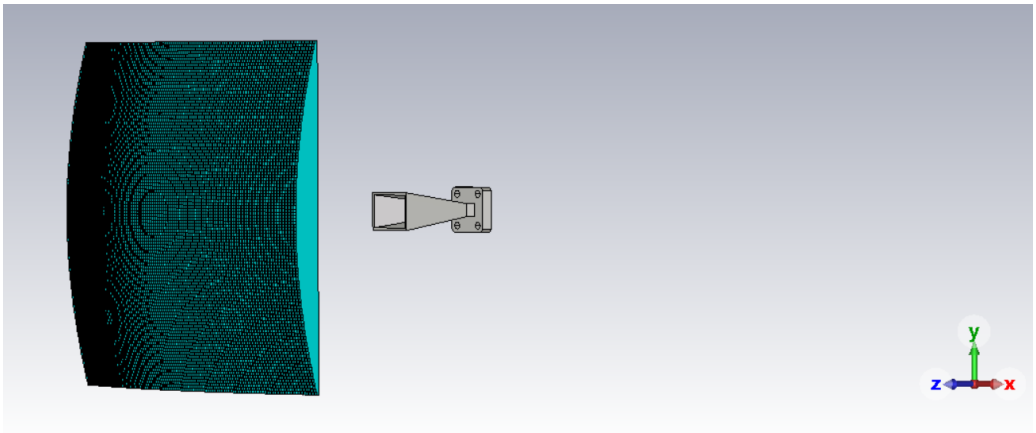
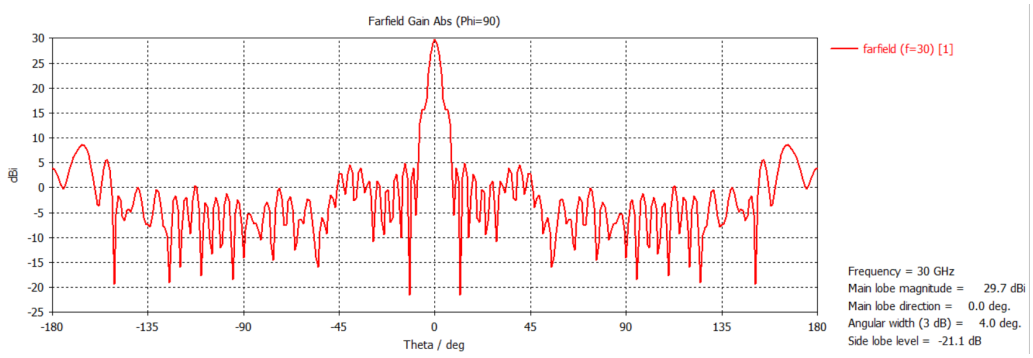
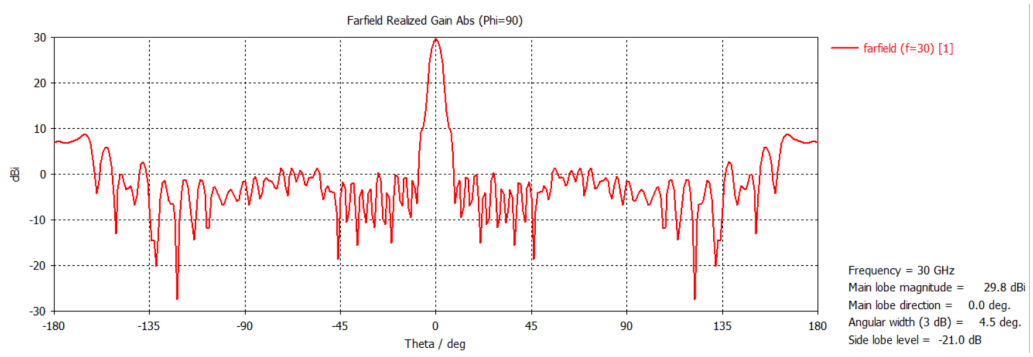


FIGURE 3.9. Discrete lens designed with $\varepsilon_r = 7.5$ using $\lambda/8$ discretization, showing the horn feed and lens geometry.

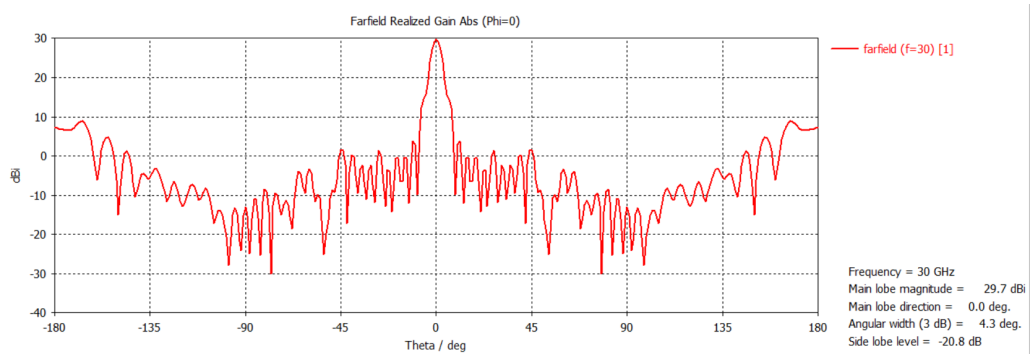
Each of the designs shown in Figures 3.7, 3.8, and 3.9 were simulated in CST Microwave Studio using the same dielectric material ($\varepsilon_r = 7.5$), feed horn, and focal distance as in the continuous lens model. The goal of these simulations is to analyze how the discretization level $\lambda/2$, $\lambda/4$, and $\lambda/8$ affect the overall performance of the lenses and compare the results with the continuous lens.



(A) $\lambda/2$ discretization.



(B) $\lambda/4$ discretization.



(C) $\lambda/8$ discretization.

FIGURE 3.10. Far-field radiation patterns of discrete dielectric lenses with different discretization levels: (a) $\lambda/2$, (b) $\lambda/4$, and (c) $\lambda/8$.

Figure 3.10 presents the simulated far-field radiation patterns of the discrete dielectric lenses at 30 GHz, for three different discretization levels ($\lambda/2$, $\lambda/4$, and $\lambda/8$). All three configurations successfully collimate the radiation from the horn feed into a highly directive beam centered at 0°, confirming that the discrete lenses effectively reproduce the required aperture phase distribution derived from the continuous model.

For the $\lambda/2$ discretization, the lens achieves a peak gain of 29.7 dBi with a 3 dB beamwidth of 4.0°, and sidelobe levels of –21.1 dB.

In the $\lambda/4$ discretization, the main beam remains centered and narrow, with a peak gain of 29.8 dBi and a 3 dB beamwidth of 4.5°. However, some small secondary lobes appear close to the boresight, which slightly increases the overall sidelobe level. This

behavior may be linked to periodicity effects at this specific discretization level, suggesting that $\lambda/4$ may not represent an optimal periodicity for the chosen operating frequency.

For the $\lambda/8$ discretization, the radiation pattern exhibits a gain of 29.7 dBi, a beamwidth of 4.3°, and sidelobe levels of –20.8 dB, comparable to those of the $\lambda/2$ lens.

The sidelobe levels seen in the radiation patterns are mainly attributed to reflections occurring at the air–dielectric interfaces. These reflections are visible in Figure 3.10 near $\theta = -180°$ and $\theta = 180°$. These effects come from the high dielectric permittivity of the lens material, which increases the impedance mismatch between the lens and the surrounding medium (air), leading to wave reflections in the far-field pattern.

To make the comparison between the different discretization levels clearer, Figure 3.11 presents the far-field radiation patterns of the three discrete dielectric lenses ($\lambda/2$, $\lambda/4$, and $\lambda/8$) in a single plot.

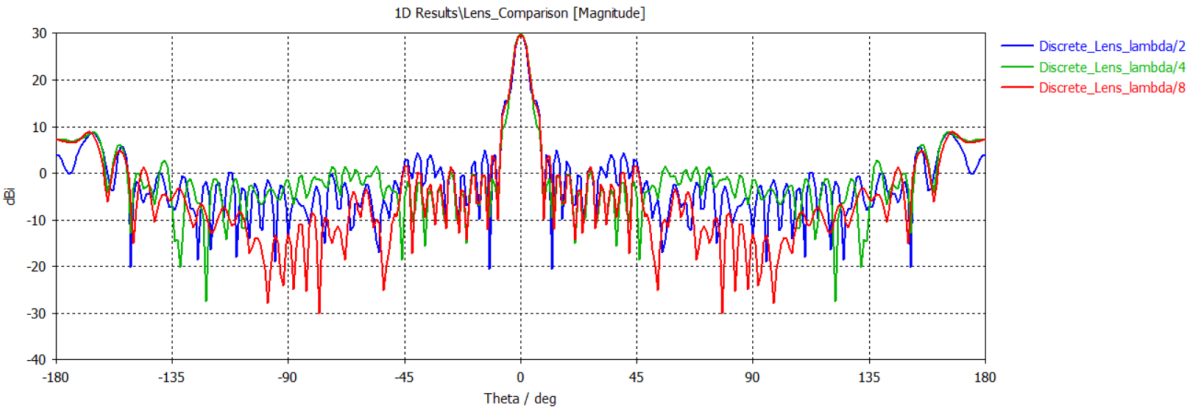


FIGURE 3.11. Comparison of the far-field radiation patterns of discrete dielectric lenses with different discretization levels ($\lambda/2$, $\lambda/4$, and $\lambda/8$) at 30 GHz.

Overall, these results confirm that the discrete lens can effectively reproduce the desired aperture phase distribution, forming a highly directive beam with good sidelobe levels. Small variations in gain and sidelobe levels across the different discretization levels reveal the influence of discretization on performance. To better understand how these lenses perform beyond the design frequency, the next step is to analyze their broadband behavior across the operating band (26 – 36 GHz).

Before analyzing the broadband performance of the discrete lenses, it is important to include the continuous lens as a reference. The continuous model represents the ideal case, where the phase profile is perfectly smooth across the aperture. By comparing its frequency response with that of the discretized designs, it becomes possible to evaluate how the phase distribution accomplished by the UC periodicity affects the overall bandwidth and realized gain of the lens.

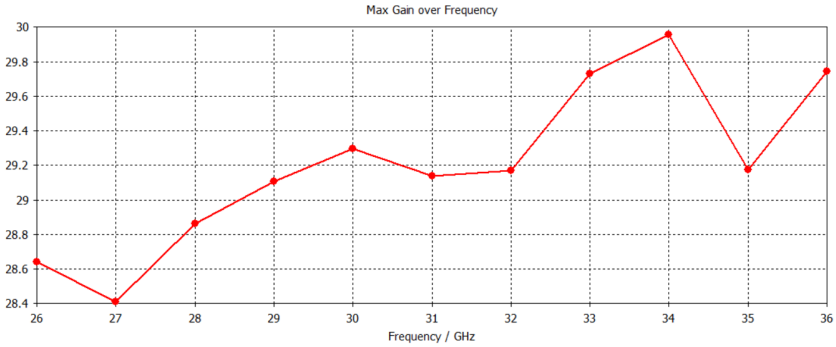
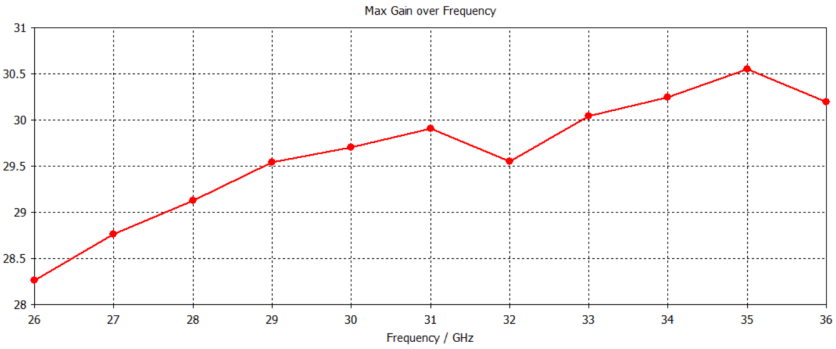
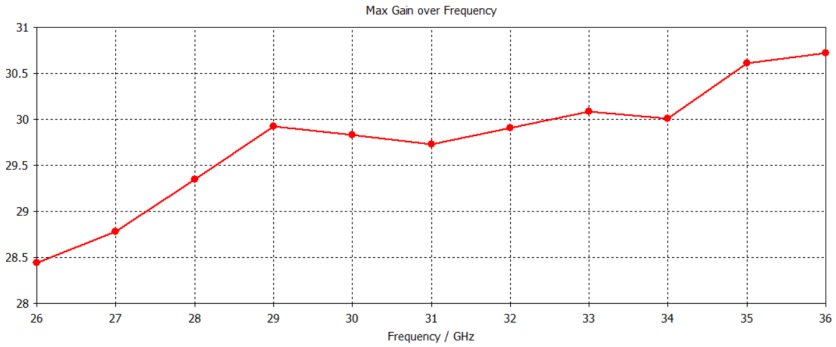


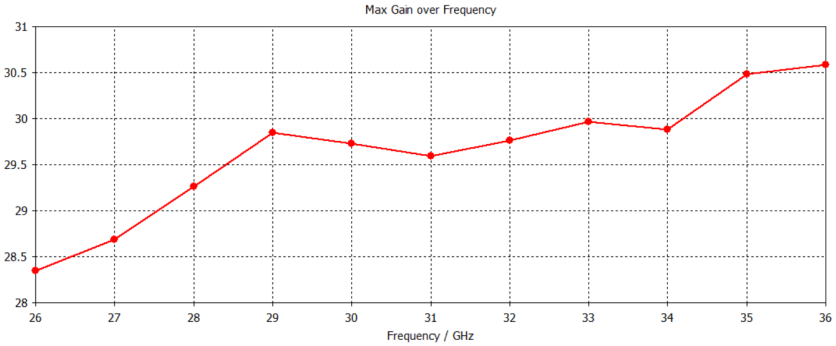
FIGURE 3.12. Simulated broadband gain response of the continuous dielectric lens across the 26–36 GHz frequency range.



(A) Discrete lens with $\lambda/2$ discretization.



(B) Discrete lens with $\lambda/4$ discretization.



(C) Discrete lens with $\lambda/8$ discretization.

FIGURE 3.13. Simulated broadband gain response of the discrete dielectric lenses across the 26–36 GHz frequency range for different discretization levels.

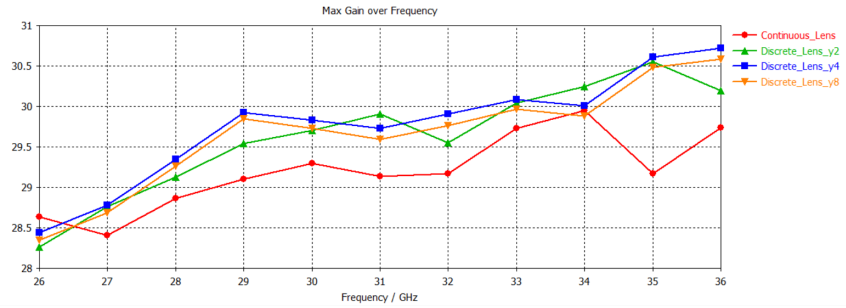


FIGURE 3.14. Simulated broadband gain response of the continuous and discrete dielectric lenses across the 26–36 GHz frequency range.

Figure 3.12 shows the simulated broadband gain response of the continuous dielectric lens across the 26–36 GHz frequency band. The gain remains relatively stable throughout the entire frequency range, with a slight increase as frequency rises, reaching a maximum value of around 29.9 dB at 34 GHz. This result confirms that the continuous lens maintains a consistent performance within the operating frequency range.

The same broadband analysis was carried out for the discrete lenses, and the corresponding results are presented in Figure 3.13.

Figure 3.13 shows the simulated broadband gain response of the discrete dielectric lenses across the 26–36 GHz frequency band for three different discretization levels ($\lambda/2$, $\lambda/4$, and $\lambda/8$). All three lenses maintain a high gain over the entire operating frequency range.

For the $\lambda/2$ discretization, the gain increases steadily with frequency, reaching a maximum of 30.56 dB at 35 GHz. The $\lambda/4$ discretization exhibits a peak gain of 30.72 dB at 36 GHz. Similarly, the $\lambda/8$ discretization provides an identical result, achieving a peak of 30.58 dB at 36 GHz. All curves show very similar results, indicating that within this frequency range, the discretization level does not significantly affect the overall performance of the lenses.

Interestingly, the $\lambda/4$ and $\lambda/8$ lenses exhibit nearly identical trends across the frequency band, following the same variations in gain with the only noticeable difference being the absolute gain value, which is slightly lower for the $\lambda/8$ case.

Another observation is the presence of a small secondary curvature in the far-field pattern of the continuous lens near the boresight region (approximately between $-100°$ and $100°$). This curvature becomes more apparent as the discretization level increases. While it is barely noticeable for the $\lambda/2$ and $\lambda/4$ lenses, it becomes more distinct in the $\lambda/8$ case. This effect happens due to the smaller steps of the UCs that more accurately mimics the contiunous profile. Figure 3.15 compares the far-field radiation patterns of the continuous and $\lambda/8$ lenses, highlighting this behavior.

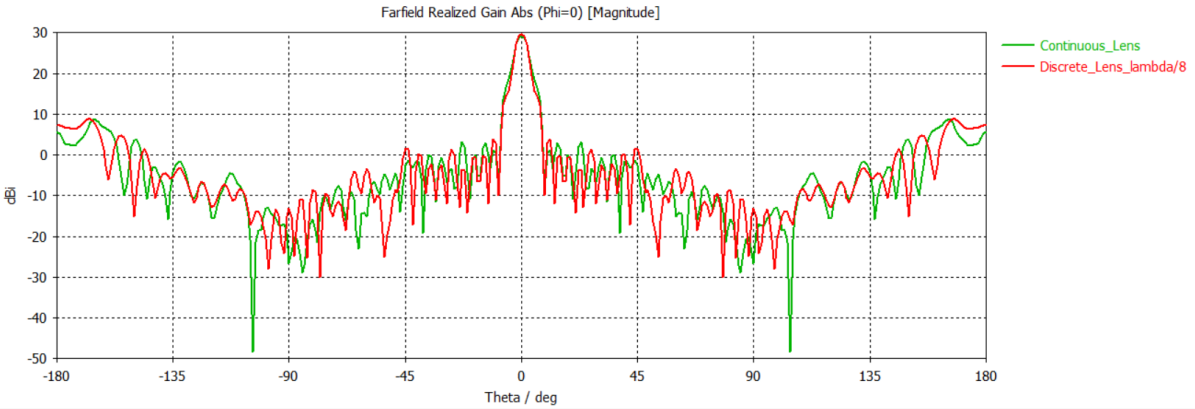


FIGURE 3.15. Comparison between the far-field radiation patterns of the continuous and $\lambda/8$ discrete dielectric lenses at 30 GHz.

The results presented in this section demonstrate that both the continuous and discrete dielectric lenses achieve the desired beam collimation, confirming that the designed phase profiles transforms the spherical wavefront from the horn feed into a highly directive beam. The continuous lens can be seen as an ideal reference, showing a smooth phase progression and good broadband performance. The discrete implementations, built from unit cells with different discretization levels ($\lambda/2$, $\lambda/4$, and $\lambda/8$), reproduce the same electromagnetic behavior with only small variations in gain and sidelobe level. This confirms that the discretization process preserves the characteristics of the continuous lens. The broadband analysis confirmed that all discrete lenses maintained a nearly identical performance across the 26–36 GHz band, indicating that even coarser discretizations ($\lambda/2$) are able to achieve good results in this frequency range.

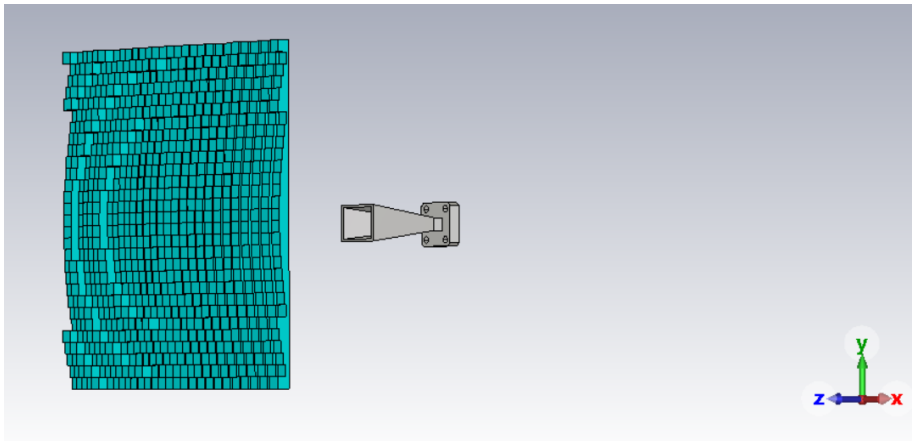
These results confirm the discrete lens approach can have a very similar performance compared with the continuous lens. However, while the discrete design reproduces the desired phase distribution effectively, the resulting lenses remain relatively thick even though a high dielectric material is used. To address this limitation, the next section introduces the zoned lens, which uses phase wrapping which significantly reduces the structure thickness.

3.4. Zoned Lens

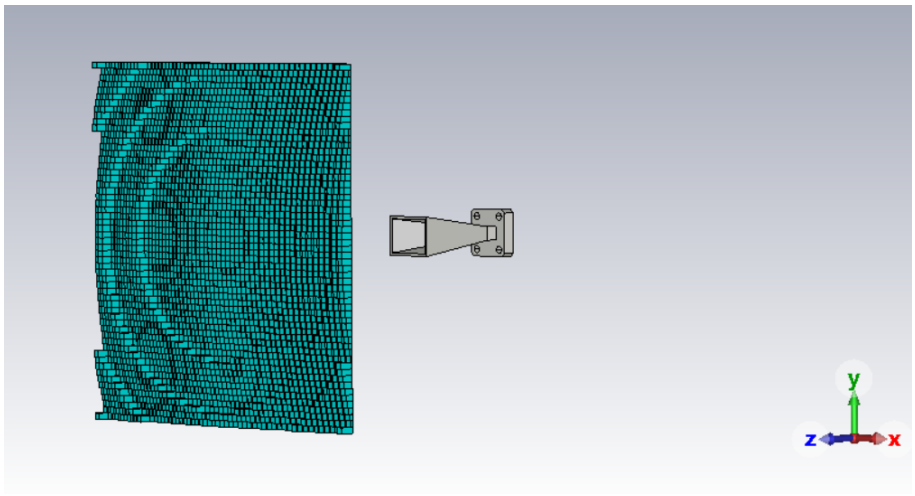
The results obtained from the continuous and discretized lens models has demonstrated that both approaches are capable of producing directive beams. These configurations, however, require a large lens thickness to achieve the required phase compensation across the aperture. At high frequencies, such as in MMW applications, this can lead to bulky structures, even when using high permittivity materials. Another approach that can reduce the overall lens thickness is the zoned lens.

The zoned lens is based on the concept of phase wrapping. Phase wrapping happens when the phase value exceeds 2π and cycles back to 0. In this way, it is possible to control and limit the lens thickness. This effectively folds the lens into a thinner geometry without altering the overall phase distribution at the aperture. The phase jumpes introduced

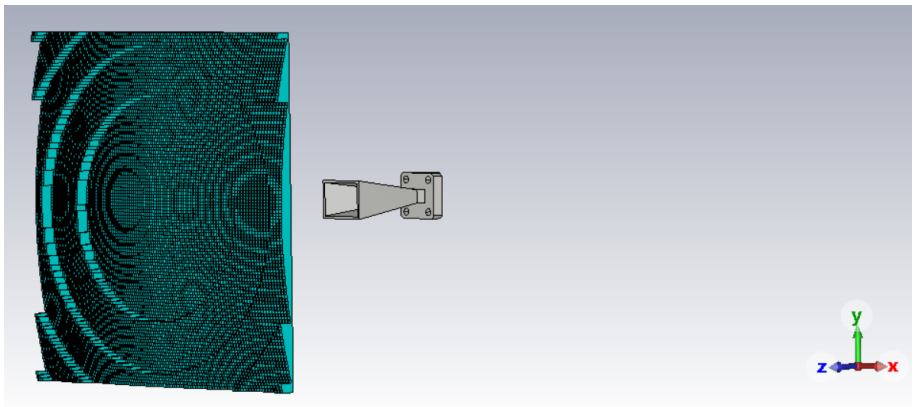
by zoning do not change the beam direction or focusing condition, but it reduces the physical thickness of the lens. This provides a compact and lightweight alternative to the conventional continuous or discrete dielectric profiles. The thickness of these lenses is $0.6\lambda_0$.



(A) $\lambda/2$ discretization



(B) $\lambda/4$ discretization



(C) $\lambda/8$ discretization

FIGURE 3.16. Zoned lenses designed for different discretization levels using $\varepsilon_r = 7.5$, showing the horn feed and lens arrangement: (a) $\lambda/2$, (b) $\lambda/4$, and (c) $\lambda/8$.

The main advantage of this method is the reduction in height, which simplifies fabrication. However, because the phase profile is now discontinuous, the zoned lens can exhibit shadow losses and reduced operational bandwidth [4].

In this section, several zoned lenses were designed using the same dielectric permittivity ($\varepsilon_r = 7.5$), but with different discretization levels ($\lambda/2$, $\lambda/4$, and $\lambda/8$). Each configuration was implemented in CST Microwave Studio with the same feed horn and focal length used in the previous designs. Figure 3.16 illustrates the resulting geometries for the three discretization levels, showing both the lens and the feed.

Each of the zoned lenses presented in Figure 3.16 was designed using a UC based approach, in which the phase distribution across the aperture is synthesized by varying only the height of dielectric TAs. This design strategy directly links the lens to the concept of a discrete TA, where each cell introduces a specific phase delay according to its height or geometry.

The UCs were arranged with a periodicity determined by the selected discretization level. For the three case studies, the periodicities correspond to $\lambda/2 = 5\,\text{mm}$, $\lambda/4 = 2.5\,\text{mm}$, and $\lambda/8 = 1.25\,\text{mm}$, respectively, at the design frequency of 30 GHz. A finer discretization (smaller periodicity) results in a closer approximation to the continuous phase profile, at the expense of a higher number of UC.

With these lenses defined, the next step was to evaluate their electromagnetic performance. The simulated far-field radiation patterns at the design frequency of 30 GHz are presented and compared to assess the effect of discretization level on beam collimation and gain.

The electromagnetic performance of the zoned lenses was first evaluated at the design frequency of 30 GHz to assess the impact of discretization level on beam collimation, gain, and sidelobe levels. Each simulation used the same feed horn and focal distance as in the previous section.

The far-field radiation patterns for the three zoned lenses with discretization levels of $\lambda/2$, $\lambda/4$, and $\lambda/8$ are shown in Figure 3.17.

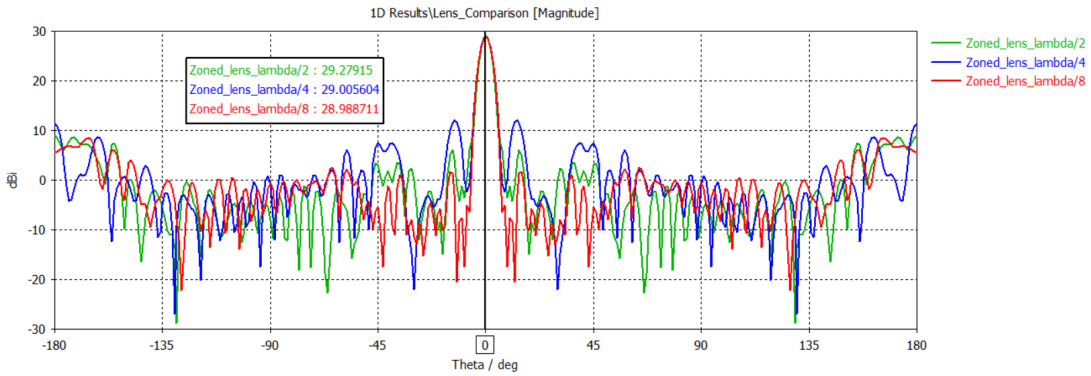
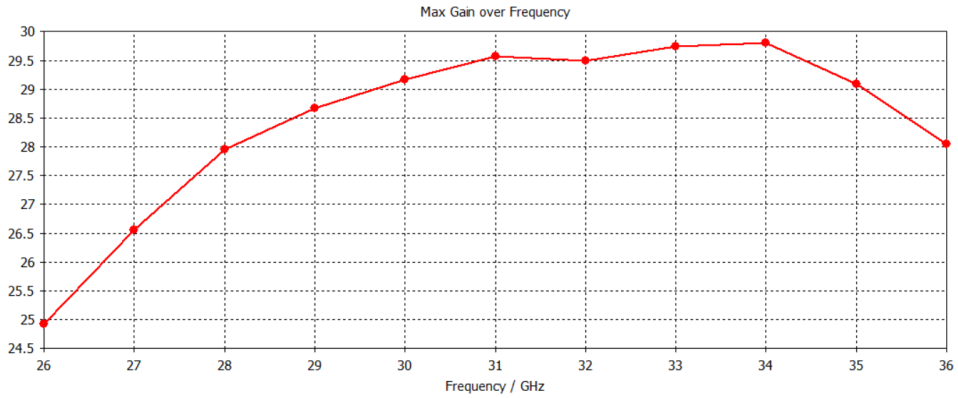


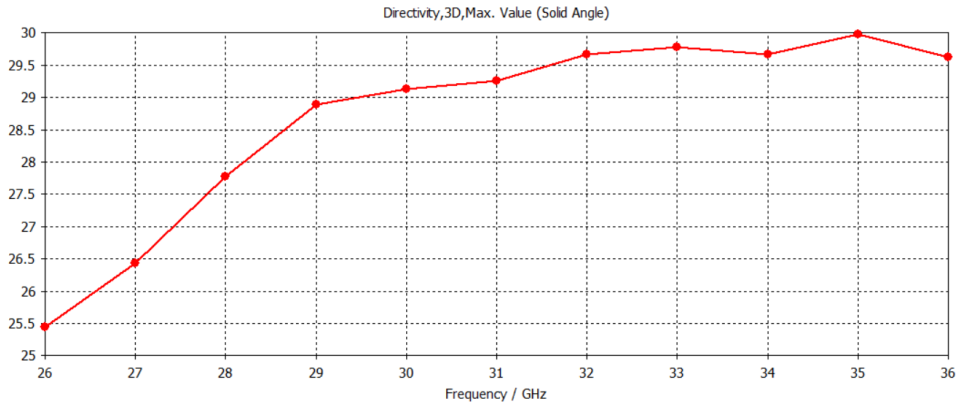
FIGURE 3.17. Comparison of the radiation pattern of zoned lenses .

Figure 3.17 presents the far-field radiation patterns of the three zoned lenses at 30 GHz, corresponding to discretization levels of $\lambda/2$, $\lambda/4$, and $\lambda/8$.

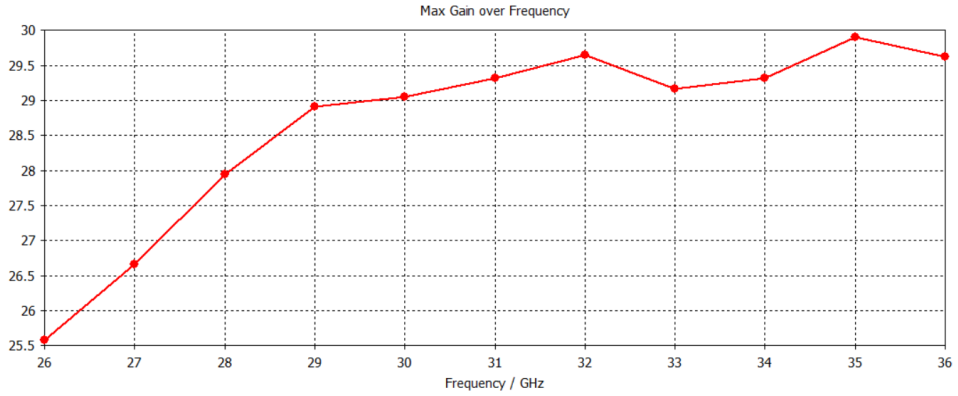
All three configurations successfully collimate the radiation from the horn feed into a directive beam centered at 0°, demonstrating that the zoning technique preserves the focal properties of the lens despite the phase discontinuities introduced by the wrapping process. Nevertheless, as the discretization becomes finer, clear differences in beam shape and sidelobe behavior can be observed.



(A) Zoned lens with $\lambda/2$ discretization.



(B) Zoned lens with $\lambda/4$ discretization.



(C) Zoned lens with $\lambda/8$ discretization.

FIGURE 3.18. Simulated far-field radiation patterns across the 26–36 GHz band for zoned lenses with different discretization levels.

For the $\lambda/2$ discretization, the lens achieved a peak gain of 29.3 dB with a 3 dB beamwidth of 4.3°. The main beam remains aligned with the boresight, as expected,

showing that the phase across the aperture is maintained. The sidelobes appeared with a level of –20.3 dB.

For the $\lambda/4$ discretization, the lens achieved a peak gain of 29.0,dBi with a 3,dB beamwidth of 4.7° and a sidelobe level of –16.8 dB.

The $\lambda/8$ zoned lens, shows a peak gain of 29.6 dBi and a 3 dB beamwidth of 4.6°. The sidelobes remained similar to the previous lenses, showing a level of –20.4 dB.

Increasing the discretization level enhances phase accuracy and sidelobe performance, but at the expense of a larger number of UCs and higher fabrication complexity. However, in Figure 3.17 it can be seen that for $\lambda/4$ there are two secundary lobes close to boresight. These secundary lobes can also be seen for $\lambda/2$ and $\lambda/8$, they are however smaller when increasing the discretization level. But for $\lambda/4$ this is not observed. A possible explination, is that for this working frequency $\lambda/4$ is not ideal, and optimazing the discretization level could result in a better gain and sidelobe levels.

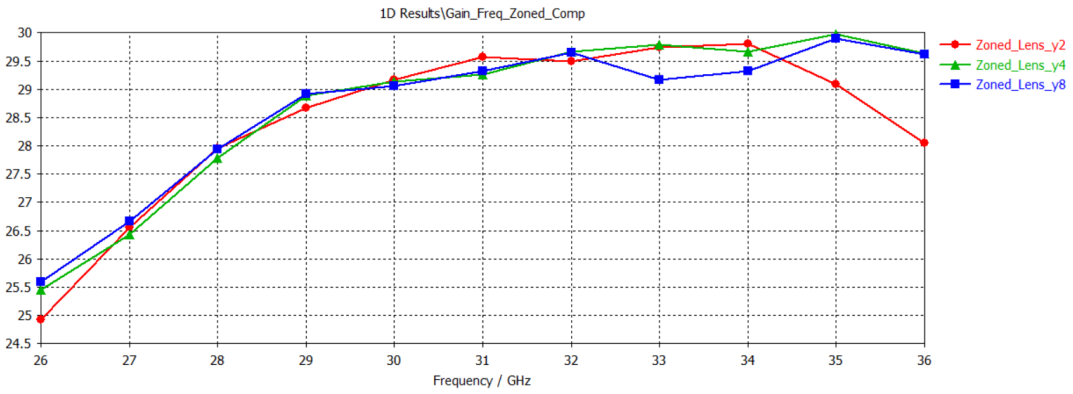


FIGURE 3.19. Simulated broadband gain response across the 26–36 GHz band for zoned lenses with different discretization levels.

While the previous analysis focused on the lens performance at the design frequency of 30 GHz, it is also important to evaluate how each lens behaves over a wider frequency range.

To investigate this, all three zoned lens configurations were simulated across the 26–36 GHz band. By comparing the $\lambda/2$, $\lambda/4$, and $\lambda/8$ discretizations over the band, it becomes possible to quantify how the level of zoning influences the operational bandwidth.

Figure 3.18 presents the simulated far-field results for the three zoned lenses across the 26–36 GHz frequency band. All three lenses exhibit consistent performance over the operating range, maintaining a high gain across the frequency band.

For the $\lambda/2$ discretization, the gain increases steadily up to 31 GHz, stabilizing and reaching a maximum of approximately 29.80 dB at 34 GHz before decreasing.

The $\lambda/4$ lens shows slightly better results, achieving a peak gain of 29.97 dB at 35 GHz. However, the curve remains more stable across the band, which may suggest that this

discretization offers a better overall performance compared to $\lambda/2$, despite the small secondary lobes observed at 30 GHz.

For the $\lambda/8$ discretization, the lens presents similar results, maintaining a constant increase in gain across most of the frequency range, as also seen in the $\lambda/4$ case, with only minor fluctuations. The peak gain achieved was 29.90 dB at 35 GHz.

Similar to what was observed in the discrete dielectric lenses, the sidelobe levels in the zoned configurations are mainly attributed to reflections at the air–dielectric interfaces. These reflections are particularly noticeable near $\theta = -180°$ and $\theta = 180°$ in the far-field patterns.

Overall, while all three configurations perform well across the 26–36 GHz band, the $\lambda/4$ and $\lambda/8$ lenses provide the most stable and higher gain responses, demonstrating that finer discretization improves not only sidelobe levels but also the overall bandwidth and gain of zoned dielectric lenses.

The results discussed throughout this chapter have shown how dielectric phase control can be implemented through progressively more complex structures, from the UC model, to the basic slab model, and finally to the discretized and zoned lenses. By comparing these designs, the zoned approach, while reducing lens thickness and overall volume, introduces limitations in terms of bandwidth performance.

While both configurations maintain a high gain around the design frequency, the discrete lens exhibits a broader operational frequency range. In contrast, the zoned lenses show a reduction in gain as frequency increases within the considered band, resulting a narrower bandwidth. This effect is particularly noticeable for the $\lambda/2$ discretization of the zoned lens, where the gain starts to decrease after 34 GHz, while in the discrete lenses, this behavior is not observed.

These results show that even though zoned lenses are lighter and thinner, making them easier to fabricate and integrate, have a narrower operational bandwidth. Discrete dielectric lenses, on the other hand, maintain more consistent gain throuhtout the frequency band and have better broadband behavior.

The next chapter focuses on developing these principles into a fully engineered TA antenna. By combining the phase control studied for discrete lenses with a more flexible UC approach, where geometry can be engineered to dictate the amplitude and phase response of the cells, TAs enable a local manipulation of electromagnetic waves while maintaining a compact structure and being easy to fabricate, which is essential for MMW applications.

CHAPTER 4

Design high permittivity TA

The transition from dielectric slab model to discretized UC structures represents a critical step in the development of high performance MMW lens antennas. While the homogeneous slab analysis in Chapter 3 demonstrated the relationship between phase delay, thickness and permittivity, such geometries are insufficient for achieving the requirements of MMW systems, as observed in chapter 3.

To overcome these limitations, the central goal of this chapter is to develop and validate a library of UCs that will be used for the design of a fully dielectric TA. Each UC will be engineered to provide a specific phase delay while maintaining a good amplitude response and broad operational bandwidth. The geometry of the UC will have restrictions based on the material that is going to be used and the limitations of the 3D printer.

The second objective of this chapter is to assemble a discretized broadband TA using the UC library and adapting the concept of the Risley Prism, make a mechanical steering TA, where two TAs are stacked with a defined spacing distance between them and rotated to achieve a specific beam tilt.

4.1. UC Design

The UCs were designed based on the materials of the same company selected in Chapter 3, in this design it will be used the Zetamix ϵ filament with relative permittivity $\epsilon_r = 10$ and dielectric loss tangent $\tan\delta = 0.0011$. These structures provide controlled phase shifts across the aperture while ensuring low insertion loss and a large operational bandwidth.

The geometry of the proposed UC is illustrated in Figure 4.1. It is composed of a dielectric slab of height h and width P, perforated by two rectangular air inclusions of thickness t and width W.

The introduction of these air inclusions reduces the effective permittivity of the cell compared to the bulk material, allowing the phase response to be tuned according to the ratio of dielectric-to-air within the structure.

To construct a functional TA lens, it is necessary to develop a library of UCs capable of providing phase shifts that cover the 0°–360° range while maintaining low insertion loss and broadband operation. The performance of each UC depends on three main parameters:

- the transmission amplitude ($|S_{21}|$) at the design frequency of 30 GHz;
- the phase shift introduced by the geometry;
- the usable bandwidth, defined as the frequency range in which $|S_{21}| > -1.5$ dB.

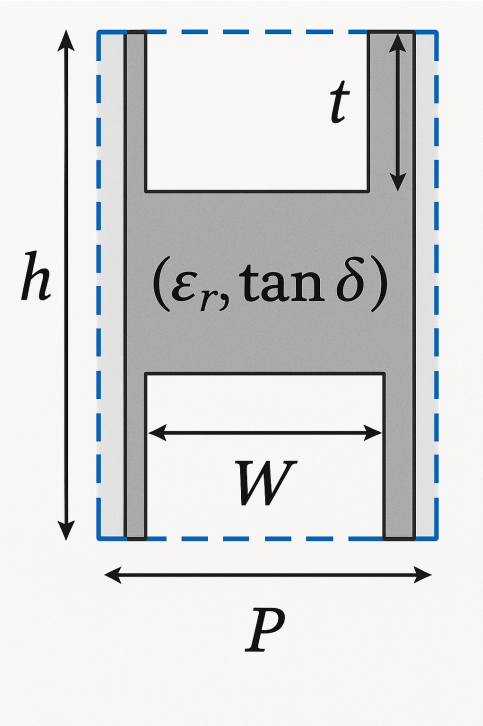


FIGURE 4.1. Proposed UC geometry [21].

By fixing the periodicity of the cells at $P = 2$ mm to avoid structural complexity, and varying the geometrical parameters h, W and t, the objective was to achieve a complete 360° phase coverage while keeping h as small as possible and ensuring broadband performance.

The results are presented in Figures 4.2 and 4.3, which show the transmission magnitude (S_{21}) and the corresponding phase response of the candidate UCs, respectively.

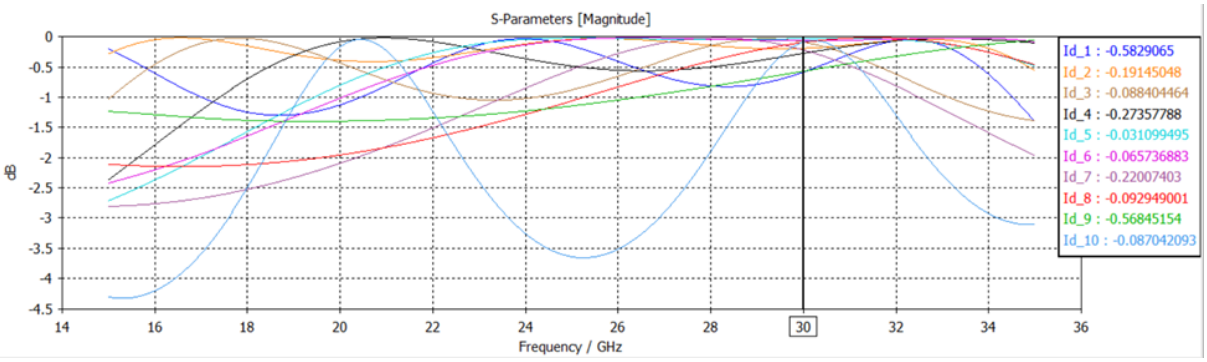


FIGURE 4.2. Transmission magnitude (S_{21}) of chosen UC.

The results in Figure 4.2 show that all of the investigated UCs achieve transmission values above -1.0 dB at the design frequency of 30 GHz, which was one of the primary goals of the design process. While a larger pool of candidate geometries was initially available, the selection prioritized broadband performance over small improvements at the design frequency.

It is important to note that increasing the height of the UCs could, in principle, extend the range of achievable phase delays and potentially improve both amplitude response and bandwidth. However, this option was discarded, as taller structures would contradict the requirement for compactness and manufacturability, since maintaining reduced cell height simplifies fabrication in AM.

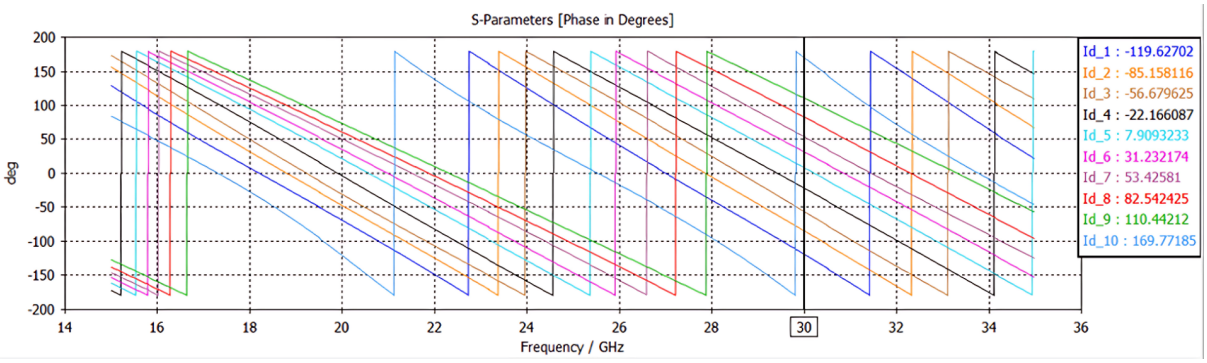


FIGURE 4.3. Phase response of candidate UCs across the frequency range.

Figure 4.3 presents the phase response of the UCs across the frequency spectrum, with the values wrapped into the $-180°$ to $180°$ interval. The set of cells nearly spans the entire $0°$–$360°$ range. The most significant discontinuity occurs between cell ID 1 and cell ID 10, where a phase gap of approximately $72°$ is observed. Although this gap is larger than the differences between other adjacent cells, it does not compromise the design.

The discontinuities observed in Figure 4.3 arise solely from the $-180°/180°$ wrapping convention and do not reflect any change in the UCs behavior. In practice, the phase of each cell evolves continuously with frequency, and the resets are simply a plotting artifact.

To provide a clearer overview of the UCs geometrical dimensions and corresponding performance, the results were consolidated in Table 4.1. The table lists, for each UC, the periodicity, height, void width, and void thickness, together with the simulated transmission coefficient, phase response at 30 GHz, as well as the bandwidth at which the transmission coefficient remains above -1.5 dB.

From Table 4.1 it can be seen that the tallest UC has a height of 5.2 mm, while the shortest measures 2.2 mm. These values are within the expected design range. All of the selected cells also show good transmission performance, with amplitude responses better than -0.6 dB at 30 GHz, ensuring that insertion losses remain low and bandwidth sufficiently wide. Only ID 10 exhibits a bandwidth below 10 GHz.

TABLE 4.1. Library of simulated UCs with corresponding geometry, transmission coefficient at 30 GHz (S_{21}), phase shift, and bandwidth (BW).

ID	P (mm)	h (mm)	W (mm)	t (mm)	S21 (dB)	Phase (°)	BW (GHz)
1	2.00	5.00	1.40	1.40	-0.58	-120	20.0
2	2.00	5.20	1.60	1.60	-0.19	-85.2	20.0
3	2.00	4.00	1.40	1.20	-0.09	-56.7	20.0
4	2.00	4.00	1.60	1.20	-0.27	-22.2	18.5
5	2.00	3.80	1.60	1.40	-0.03	7.9	19.1
6	2.00	3.60	1.60	1.50	-0.07	31.2	17.5
7	2.00	2.20	1.20	1.20	-0.22	53.4	11.8
8	2.00	2.20	1.40	1.20	-0.09	82.5	12.2
9	2.00	2.20	1.60	1.20	-0.57	110	20.0
10	2.00	5.00	1.00	0.60	-0.06	169	3.8

Within the selected set, two different types of geometry can be distinguished. The first type corresponds to the configuration shown earlier in Figure 4.1, where the inclusions are confined within the dielectric. The second type, observed in ID 7, ID 8, and ID 9, occurs when the parameter t is half of the cell height, producing a fully perforated structure with an air channel through the center.

In summary, the UC library developed achieves the requirements of phase coverage, low insertion loss, and acceptable bandwidth for operation around 30 GHz. While each cell was studied in isolation under periodic boundary conditions, their practical utility lies in how they can be arranged together to synthesize a complete phase distribution across an aperture. The next step, therefore, is to assemble these UCs into a full TA lens, where their individual responses are combined to transform a spherical wavefront of a horn feed into a highly directive beam. This process, along with the resulting performance, is presented in Section 4.2.

4.2. TA Design

With the library of UCs established in Section 4.1, the next step is the design of the complete TA capable of collimating and steering the radiation from a horn feed. Each UC provides a specific phase delay at the design frequency of 30 GHz, and by arranging them across the aperture of the TA, the required phase distribution can be synthesized, transforming the spherical wavefront into a planar or, in this case, tilted wavefront, forming a highly directive beam.

The required phase distribution across the aperture can be expressed as:

$$\phi_{\text{Lens}}(x, y) = k_0\sqrt{x^2 + y^2 + F^2} - k_0 x \sin(\alpha_0) \tag{4.1}$$

where k_0 is the free-space wavenumber, (x, y) is the position of the UC in the aperture plane, F is the focal distance (fixed at 100 mm), and α_0 defines the beam tilt angle. In this work, the TA was designed for a beam tilt of 24°, meaning that the aperture is designed to collimate the horn feed into a directive beam pointing in that direction. The lens has a diameter of 140 mm and a thickness of $0.52\lambda_0$.

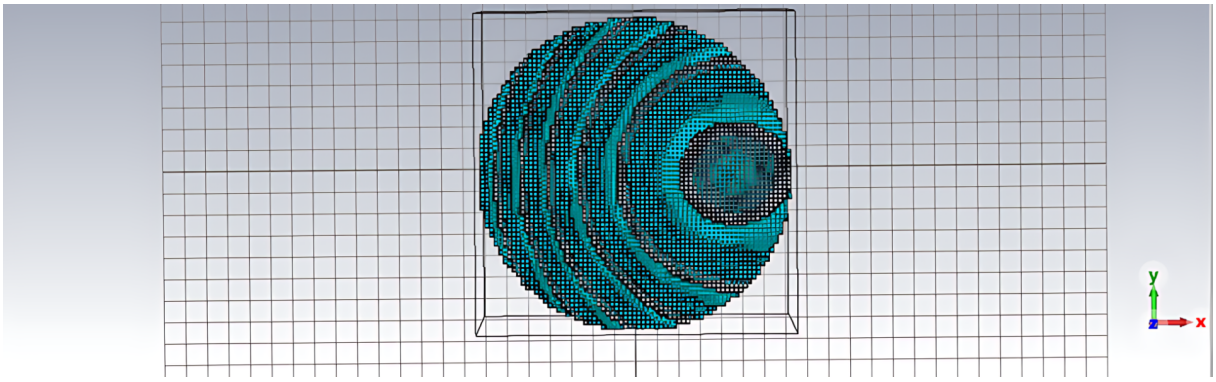


FIGURE 4.4. Final TA layout constructed with the selected UCs.

The array was fed by a standard horn antenna with a gain of 14.5 dBi, and the realized gain of the overall system is presented in Figure 4.5.

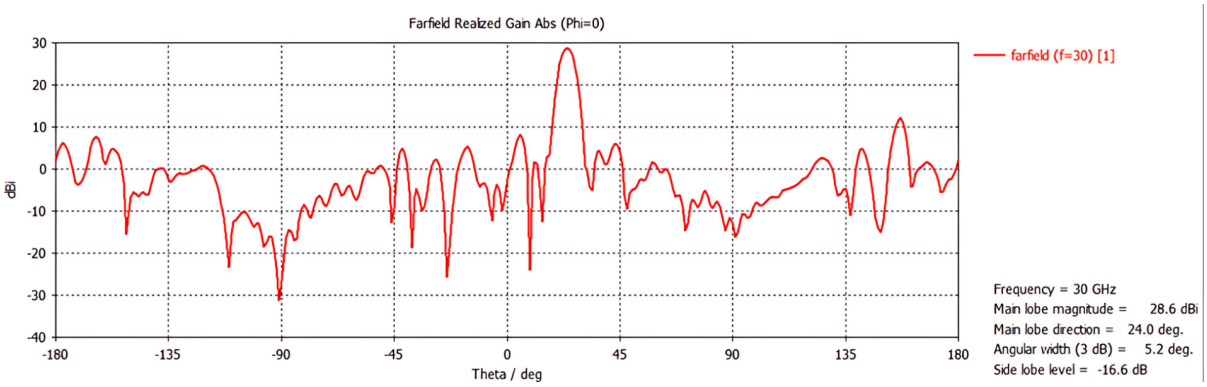


FIGURE 4.5. Realized gain pattern of the TA at 30 GHz.

Figure 4.5 shows the realized gain pattern of the structure at 30 GHz. The main lobe is observed at the expected angle of 24°, with a realized gain of 28.6 dBi. The 3 dB beamwidth is approximately 5.2°, confirming the narrow-beam behavior expected from a high directivity lens antenna and the sidelobe level is −16.6 dB.

It is also worth noticing that the sidelobe levels observed in Figure 4.5 are mainly reflections at the air–dielectric interface. In the earlier dielectric lens designs, the main beam was directed at the boresight, making these reflections appeared symmetrically around $\theta = \pm 180°$. However, since the TA is designed to make the main beam tilt by 24°, the reflections also shift accordingly, appearing near $(180° - \alpha_0)$. This can be observed in the radiation pattern of Figure 4.5.

This verifies that the UC library provides good control over the aperture phase distribution to form a well-defined beam in the desired direction.

To evaluate the broadband behavior of the TA, the frequency response was simulated between 27 and 34 GHz. The maximum realized gain in this frequency band is shown in Figure 4.6. Although the lens was designed for 30 GHz, the peak gain occurs at 32 GHz. This shift can be attributed to the amplitude and phase response of the UCs, that changes with frequency. Additionally, the beam pointing angle exhibits frequency dependence, which is an expected characteristic of discretized dielectric structures.

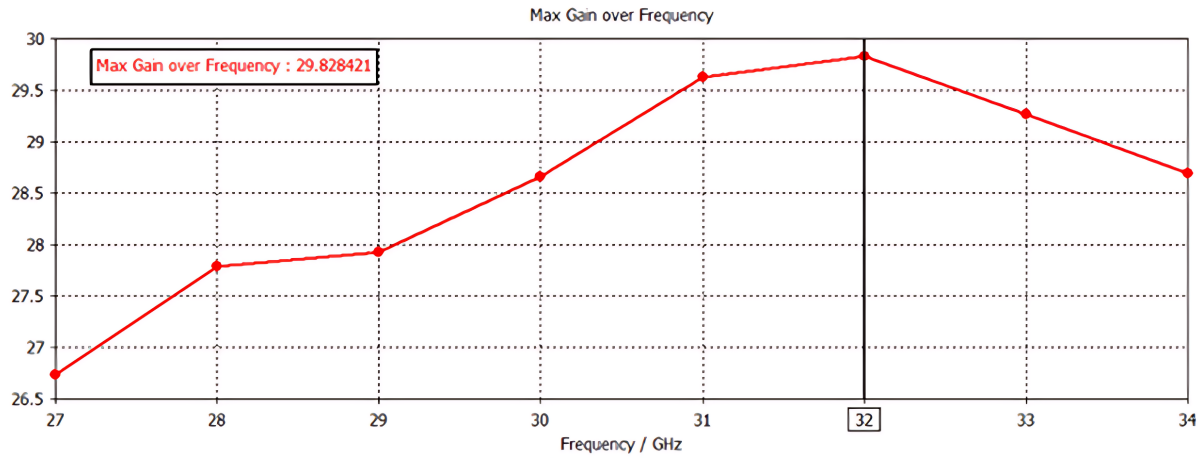


FIGURE 4.6. Maximum realized gain of the TA in the frequency band (27–34 GHz).

While the single TA presents high realized gain and broadband performance, its function is limited to a fixed beam direction defined during the design stage. For many MMW applications, such as satellite communications, automotive radar, or point-to-point backhaul, beam reconfigurability is essential. Instead of relying on electronic elements, which add cost and complexity, an alternative is to adopt a dual lens configuration inspired by the Risley prism concept. By stacking two TA lenses with relative rotation, it becomes possible to steer the beam without active components. This approach, discussed in Section 4.3, provides a compact and efficient solution for passive beam steering using the same UC library developed in this work.

4.3. Risley Prism Implementation

As discussed in Section 4.2, the single TA achieves high gain and broadband behavior, but its beam direction is fixed once designed. This limits its use in more dynamic scenarios. In many MMW applications such as satellite user terminals, automotive radar, or point-to-point backhaul links, there is a need for beams that can be steered or adjusted. Phased arrays are a used option, but these bring constraints like cost, power consumption, and overall system complexity.

An alternative is to implement the principle of the Risley prism, a concept originally developed in optics. A conventional Risley prism consists of two shaped prisms that, when rotated relative to each other, change the output beam direction. Transforming this idea to MMW antennas, two thin dielectric TA lenses can be stacked and rotated in a similar

way. The result is a passive beam steering system that maintains the simplicity and low cost of the TA approach, while enabling mechanical control of the beam direction without requiring active electronic components.

To implement the Risley prism concept using dielectric TAs, a second TA lens needs to be designed. Unlike the first TA (TA_1), which is designed to collimate and tilt the spherical wave emitted by the horn into a planar wavefront, the second TA (TA_2) is responsible only for tilting the incident wavefront by a defined angle.

This is achieved by assigning a linear phase distribution across the aperture, expressed as:

$$\phi_{\text{Lens}}(x, y) = k_0 x \sin(\alpha_0), \tag{4.2}$$

where k_0 is the free-space wavenumber and α_0 represents the desired beam tilt angle. TA_2 introduces a constant phase gradient along the x-axis, effectively steering the beam direction without modifying its collimation.

The resulting model of TA $_2$, implemented in CST Microwave Studio, is shown in Figure 4.7. The geometry is similar to that of TA_1 with the same thickness ($0.52\lambda_0$), but the imposed phase profile corresponds to the tilting function rather than focusing.

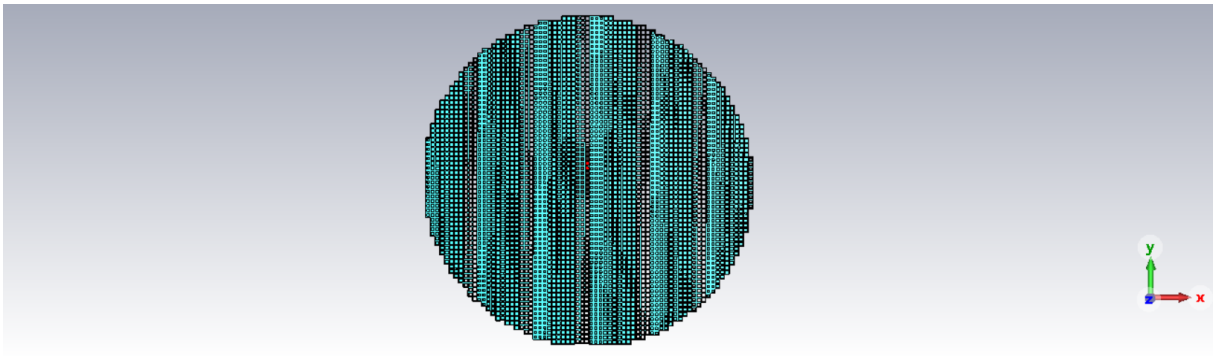


FIGURE 4.7. CST model of the tilting TA used as the second lens in the Risley prism configuration.

Although TA_2 performs a different electromagnetic function, it follows the same construction principles as TA_1 presented in the last section and is built using the same UC library introduced in Section 3.1. The only difference lies in the phase equation used during design, which results in a linear phase variation that produces the desired beam tilt instead of collimation.

When assembled, the TA system operates in two stages. TA_1 collimates the spherical wave radiated by the horn and applies a fixed beam tilt of 24°. TA_2 is placed in front of the first one with a spacing of only 1 mm, the entire structure has a thickness of $1.14\lambda_0$ and is designed to introduce an additional linear phase gradient across the aperture. By rotating TA_2 relative to TA_1, the overall beam direction is steered. This configuration effectively translates the optical Risley prism principle into the MMW antennas domain, achieving passive beam steering without any active elements.

Figure 4.8 shows the set up of the system where the horn feed illuminates TA_1 and the output beam is steered by the rotation of TA_2 and Figure 4.9 gives a 2D side view that highlights the relative thicknesses and spacing of the two TAs.

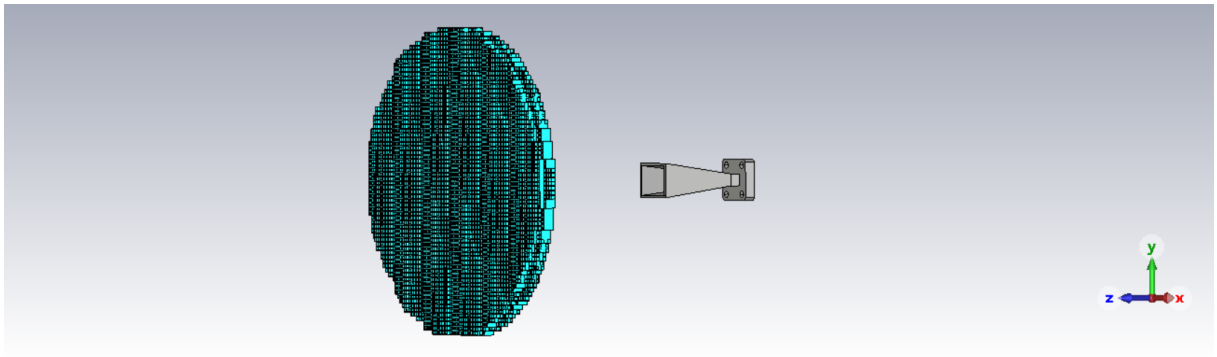


FIGURE 4.8. CST model of the Risley prism system. The horn feed illuminates TA_1, which collimates and tilts the wavefront, while the rotation of TA_2 controls the beam steering direction.

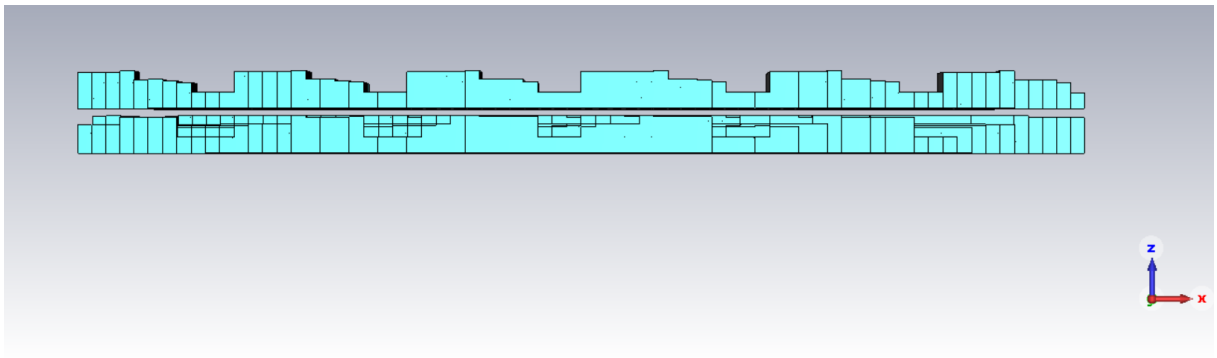
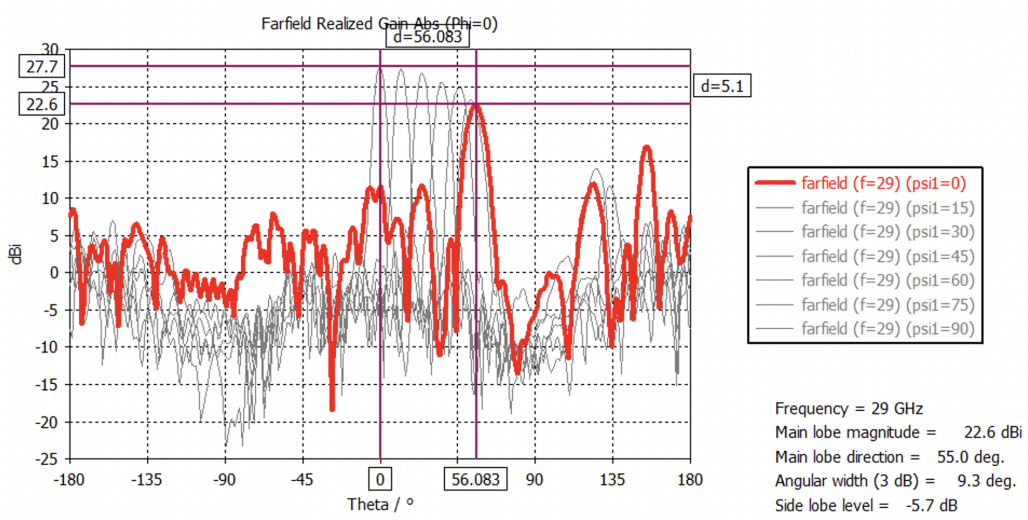
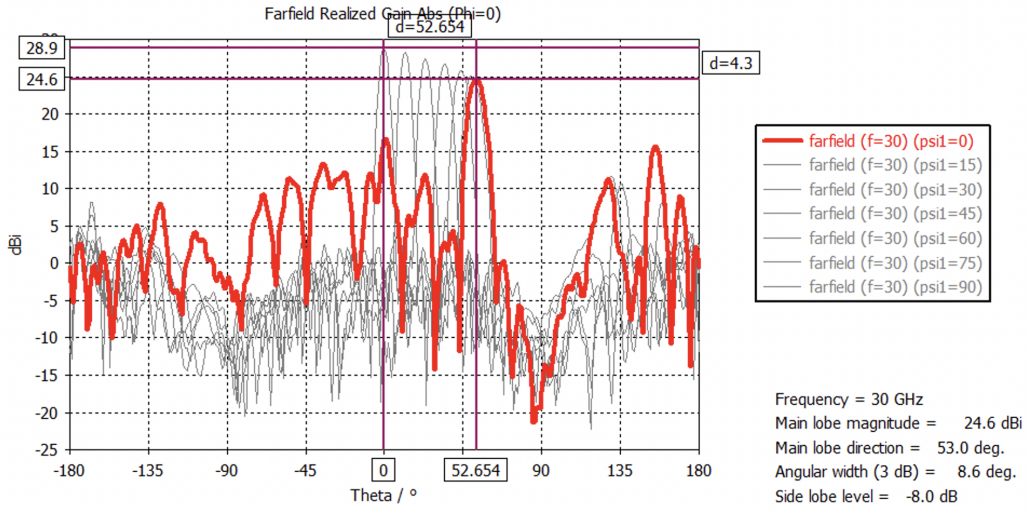


FIGURE 4.9. Side view of the Risley prism configuration showing the relative thicknesses of TA_1 and TA_2 and the 1 mm separation between them.

With the two TAs implemented, full-wave simulations were carried out in CST Microwave Studio to evaluate their beam-steering performance.During the simulations, TA_2 was rotated sequentially with respect to TA_1, while keeping the horn feed and spacing fixed. For each rotation angle, the far-field radiation pattern was computed to determine the resulting beam tilt, gain, and sidelobe level. The following figures present the simulated far-field radiation patterns and gain for different rotation angles, illustrating the beam steering effect achieved through mechanical rotation.



(A) Far-field radiation patterns at 29 GHz for different rotation angles of TA_2.



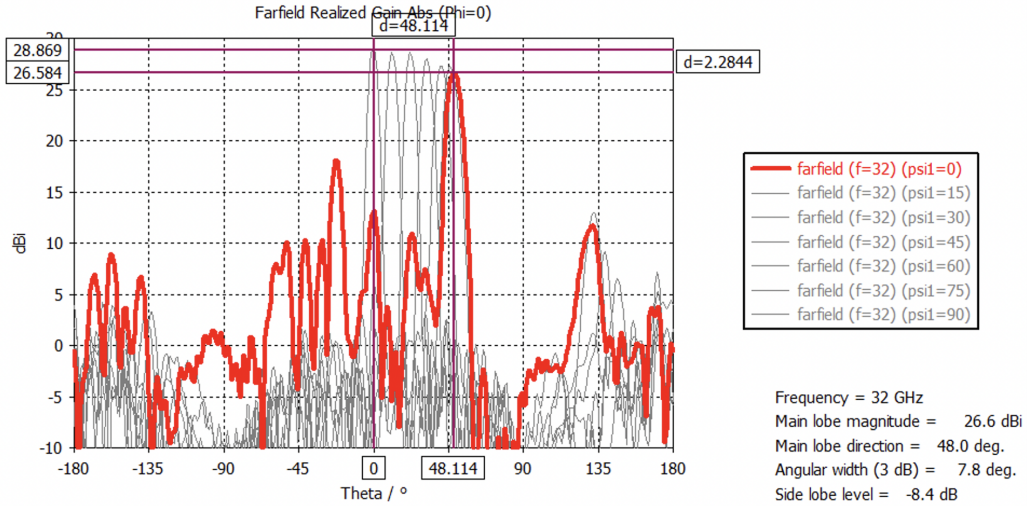
(B) Far-field radiation patterns at 30 GHz for different rotation angles of TA_2.

FIGURE 4.10. Simulated far-field radiation patterns of the Risley prism at 29 and 30 GHz for different rotation angles of TA_2.

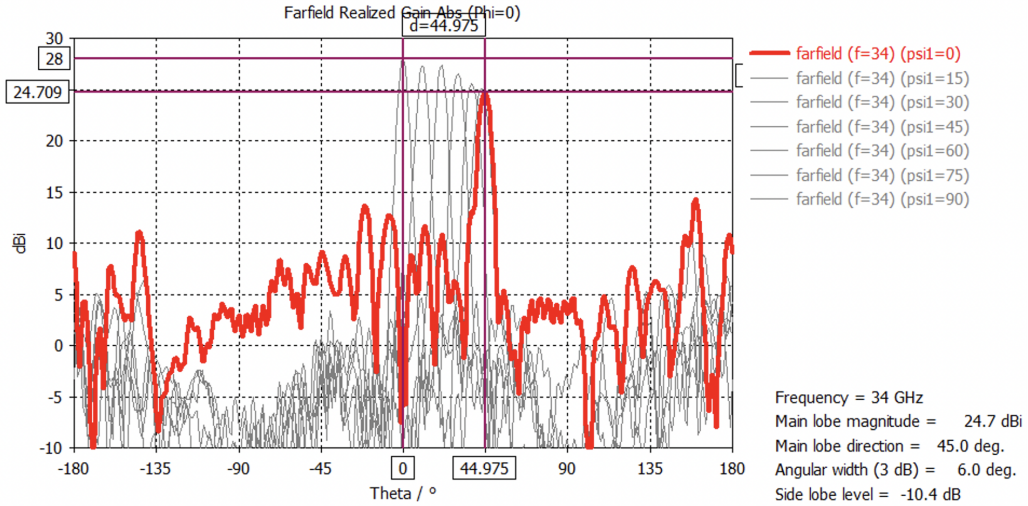
Figure 4.10 presents the simulated far-field radiation patterns of the Risley prism at 29 GHz and 30 GHz for several rotation angles of TA_2. At 29 GHz, the main beam has a maximum tilt of 56°, with a peak realized gain of 22.6 dBi and a 3 dB beamwidth of 9.3°. The sidelobe level reaches –5.7 dB, At 30 GHz, the beam reaches a maximum tilt of 52.6°. The realized gain increases to 24.6 dBi, with a 3 dB beamwidth of 8.6° and sidelobe level –8.0 dB.

Figure 4.11 presents the simulated far-field radiation patterns of the Risley prism at 32 GHz and 34 GHz for several rotation angles of TA_2. At 32 GHz, the main lobe is initially centered at approximately 0°, and it gradually moves toward larger angles as the rotation increases, reaching a maximum tilt of 48.11°. The realized gain is 26.58 dBi, with a 3 dB beamwidth of 7.8°, and sidelobe levels of –8.4 dB. At 34 GHz, the maximum tilt is directed

at approximately 45°. The peak realized gain is 24.70 dBi, with a 3 dB beamwidth of 6.0°, and sidelobe levels reaching –10.4 dB.



(A) Far-field radiation patterns at 32 GHz for different rotation angles of TA_2.



(B) Far-field radiation patterns at 34 GHz for different rotation angles of TA_2.

FIGURE 4.11. Simulated far-field radiation patterns of the Risley prism at 32 and 34 GHz for different rotation angles of TA_2.

Overall, the results demonstrate that this configuration effectively reproduces the Risley prism principle in the MMW domain. The progressive shift of the main beam direction with the rotation of TA_2 confirms the system capacity for beam steering. The realized gain remains high across the 29–34 GHz band, with only minor variations in sidelobe levels, that are, in general, reflections due to the high permittivity dielectric used. These findings highlight the potential of the proposed configuration as a low-cost, compact alternative to electronically controlled beam-steering systems that are expensive and complex.

The following section presents a comparative analysis between the single TA and the Risley prism configurations developed in this work, as well as other related designs found in the literature.

4.4. Comparative Analysis of Proposed Designs with other Dielectric based TAs

To assess the performance and relevance of the proposed transmitarray designs, this section presents a comparative analysis with other dielectric-based TAs reported in the literature. Two configurations from this work are considered: the single TA (TA_1) and the Risley prism configuration (TA_1+TA_2).

The comparison is made across several parameters, including operating frequency, dielectric characteristics, overall thickness, focal ratio (F/D), gain, aperture efficiency and 1-dB gain bandwidth. Tables 4.2 and 4.3 summarize the results.

TABLE 4.2. Comparison of the proposed TA designs with other dielectric based TAs.

Ref.	Freq. (GHz)	ε_r (tanδ)	Thickness (λ_0)	F/D	Max Gain (dBi)	Aperture Eff. (%)	1-dB Gain BW (%)
[37]	30	3.4 (N.A.)	3.0	1.4	25.1	40	13.3
[38]	30	2.77 (0.02)	3.3	1.0	30.7	38	21.5
[39]	60	2.9 (0.01)	2.0	0.42	23.5	20	17.0
[40]	94	2.2 / 10.2 (0.0009 / 0.002)	1.31	0.77	30.0	25	N.A.
[41]	15	6.0 (N.A.)	0.75	0.63	23.0	11	29.0
[21]	30	13.1 (0.046)	0.4	0.5	27.4	28	16.3
[Proposed]	30	10 (0.0011)	0.52	0.7	29.8	46.28	14.66

TABLE 4.3. Comparison of the proposed Risley prism configuration with other dielectric based beam steering systems.

Ref.	Freq. (GHz)	ε_r (tanδ)	Thickness (λ_0)	F/D	Max Gain (dBi)	Aperture Eff. (%)	Steering Range (°)
[24]	30	2.98 (0.0148)	2.9	0.70	26.4	21.15	55
[Proposed]	30	10 (0.0011)	1.14	0.7	29.2	40.31	48

The results presented in Tables 4.2 and 4.3 demonstrate that the proposed TA designs achieve similar or even superior performance when compared with other dielectric based implementations reported in the literature. Both the single TA and the Risley prism configurations exhibit high gain and good aperture efficiency, while maintaining a compact structure with reduced thickness.

CHAPTER 5

Conclusion and Future Work

This dissertation explored the design of high permittivity dielectric based lens antennas. Starting from controlling the phase of UCs using dielectric thickness and evolving towards more complex lens and TA systems capable of mechanical beam steering.

A initial study was done to understand how dielectric thickness and permittivity affected the phase response of UCs. From the general concept of UCs it is possible to simplify it to a slab model. From this model a relation between dielectric thickness and phase response has made. After the relation has verified various designs of dielectric lenses were studied.

The study started with the analysis of continuous, discrete, and zoned dielectric lenses, which helped establish how the phase of transmitted waves can be controlled through geometric variation (height). The results showed that discrete lenses can achieve a performance very close to the ideal continuous model, while being more practical to fabricate. However, these lenses were relatively bulky. To solve this, zoned lenses were designed as a way to reduce the overall thickness. When compared, both lenses exhibited high gain, but the zoned lenses showed a narrower bandwidth compared to the discrete ones.

A single TA was then designed using the UC library. This structure achieved a peak gain of 29.8 dBi at 32 GHz and a 1-dB gain bandwidth of 14.66%, with a total thickness of only 0.52 λ_0. These results show that implementing AM high permittivity dielectric TAs can provide high gain and broadband behavior while remaining compact, easy to produce and low cost.

To surpass the limitation of having a fixed beam direction, a Risley prism configuration was used. In this setup, one TA collimates and tilts the wave, while the second only tilts. The second TA can be rotated to steer the beam mechanically. The simulations showed a steering range of 48°, with a high gain of 29.2 dBi at 31 GHz and good performance across the 26–36 GHz band.

Although the results can be compared with other TA designs reported in the literature, it is important to note that the evaluation done in this work is based only on simulations. The proposed TAs have not yet been fabricated or measured, so experimental validation is still required to fully confirm the simulated performance.

Future Work

While the simulated results presented in this work are encouraging, there are several tasks that can be done to further improve this work. The most important step is to

fabricate and experimentally measure both the single TA and the Risley prism configuration. There has already been made contact with a company that will provide outsourcing services, in this case printing the TA.

This would allow validate the simulated performance, in terms of realized gain, bandwidth, and beam-steering, while also showing pratical challenges such as manufacturing problems, material losses and printing errors.

Another important task is the addition of new UC to the unit-cell library. Although the current set of unit cells provides a nearly complete 360° phase coverage, there are phase jumpes that are still present between adjacent cells. Developing additional intermediate geometries could help minimize these phase jumps, resulting in smoother phase transitions, improve gain, and broaden the TA bandwidth.

Furthermore, there is space to reduce the overall system thickness by exploring alternative feeding systems. In particular, replacing the horn feed with a leaky-wave or planar feed structure could lead to a more compact system better suited for space limited applications.

References

[1] D. Liu, H. Nakano, X. Qing, and T. Zwick, *Handbook of Antenna Technologies*, Z. N. Chen, Ed. Singapore: Springer, 2016.

[2] N. C. Garcia and J. D. Chisum, "High-efficiency, wideband grin lenses with intrinsically matched unit cells," *IEEE Transactions on Antennas and Propagation*, vol. 68, pp. 5965–5977, 8 Aug. 2020, ISSN: 15582221. DOI: 10.1109/TAP.2020.2990289.

[3] T. Komljenovic and Z. Sipus, "Dielectric lens antennas design at millimeter waves," in *2008 50th International Symposium ELMAR*, IEEE, 2008, pp. 27–30. DOI: 10.1109/ELMAR.2008.4747580. [Online]. Available: https://ieeexplore.ieee.org/document/4747580.

[4] C. A. Fernandes, E. B. Lima, and J. R. Costa, "Dielectric lens antennas," in Springer Singapore, 2016, pp. 1001–1064. DOI: 10.1007/978-981-4560-44-3_40. [Online]. Available: http://link.springer.com/10.1007/978-981-4560-44-3_40.

[5] M. Imbert, J. Romeu, M. Baquero-Escudero, M. T. Martinez-Ingles, J. M. Molina-Garcia-Pardo, and L. Jofre, "Assessment of ltcc-based dielectric flat lens antennas and switched-beam arrays for future 5g millimeter-wave communication systems," *IEEE Transactions on Antennas and Propagation*, vol. 65, pp. 6453–6473, 12 Dec. 2017, ISSN: 0018926X. DOI: 10.1109/TAP.2017.2767821.

[6] B. T. Malik, V. Doychinov, S. A. R. Zaidi, I. D. Robertson, and N. Somjit, "Antenna gain enhancement by using low-infill 3d-printed dielectric lens antennas," *IEEE Access*, vol. 7, pp. 102 467–102 476, 2019. DOI: 10.1109/ACCESS.2019.2931772. [Online]. Available: https://doi.org/10.1109/ACCESS.2019.2931772.

[7] A. Bansal and R. Gupta, "A review on microstrip patch antenna and feeding techniques," *International Journal of Information Technology (Singapore)*, vol. 12, pp. 149–154, 1 Mar. 2020, ISSN: 25112112. DOI: 10.1007/s41870-018-0121-4.

[8] C. A. Balanis, *Antenna Theory: Analysis and Design*, 3rd. John Wiley & Sons, 2005, ISBN: 978-0471667827.

[9] A. R. Harish and M. Sachidananda, *Antennas and wave propagation*. Oxford University Press, 2007, p. 402, ISBN: 9780195686661.

[10] J.-M. Poyanco, F. Pizarro, and E. Rajo-Iglesias, "3-d-printed integrated grin lens–polarizer using anisotropic materials," *IEEE Transactions on Antennas and Propagation*, vol. 72, no. 6, pp. 5343–5348, 2024. DOI: 10.1109/TAP.2023.3329959. [Online]. Available: https://doi.org/10.1109/TAP.2023.3329959.

[11] J. Thornton and K.-C. Huang, *Modern Lens Antennas for Communications Engineering*. Hoboken, NJ: Wiley-IEEE Press, 2013, ISBN: 978-1118010655.

[12] W. Shao, H. Sato, X. Li, K. K. Mutai, and Q. Chen, "Perforated extensible 3-d hyperbolic secant lens antenna for directive antenna applications using additive manufacturing," *Optics Express*, vol. 29, p. 18 932, 12 Jun. 2021, ISSN: 10944087. DOI: 10.1364/oe.426824.

[13] V. Komarov, S. Wang, and J. Tang, "Permittivity and measurement," *Encyclopedia of RF and Microwave Engineering*, pp. 3693–3711, Jan. 2005.

[14] S. Zhang, R. K. Arya, W. G. Whittow, D. Cadman, R. Mittra, and J. C. Vardaxoglou, "Ultra-wideband flat metamaterial grin lenses assisted with additive manufacturing technique," *IEEE Transactions on Antennas and Propagation*, vol. 69, pp. 3788–3799, 7 Jul. 2021, ISSN: 15582221. DOI: 10.1109/TAP.2020.3044586.

[15] A. O. Diallo, R. Czarny, B. Loiseaux, and S. Hole, "Comparison between a thin lens antenna made of structured dielectric material and conventional lens antennas, in q-band in a compact volume," *IEEE Antennas and Wireless Propagation Letters*, vol. 17, pp. 307–310, 2 Feb. 2018, ISSN: 15361225. DOI: 10.1109/LAWP.2017.2787789.

[16] S. Zhang, P. Liu, and W. Whittow, "Design and fabrication of 3-d-printed high-gain broadband fresnel zone lens using hybrid groove-perforation method for millimeter-wave applications," *IEEE Antennas and Wireless Propagation Letters*, vol. 21, pp. 34–38, 1 Jan. 2022, ISSN: 15485757. DOI: 10.1109/LAWP.2021.3116459.

[17] N. Muckermann, R. Schmitz, J. Barowski, and N. Pohl, "A fresnel-based lens antenna with reduced antenna reflections for millimeter wave radar," in *2024 54th European Microwave Conference (EuMC)*, IEEE, Sep. 2024, pp. 268–271, ISBN: 978-2-87487-077-4. DOI: 10.23919/EuMC61614.2024.10732805. [Online]. Available: https://ieeexplore.ieee.org/document/10732805/.

[18] K. Aljaloud, Y. T. Aladadi, M. A. S. Alkanhal, W. M. Abdulkawi, and R. Hussain, "A wideband grin dielectric lens antenna for 5g applications," *Micromachines*, vol. 14, p. 997, 5 May 2023, ISSN: 2072-666X. DOI: 10.3390/mi14050997. [Online]. Available: https://www.mdpi.com/2072-666X/14/5/997.

[19] J. A. Vasquez-Peralvo, J. M. Fernandez-Gonzalez, and T. Wong, "3d printed discrete dielectric lens with improved matching layers," Nov. 2023. [Online]. Available: http://arxiv.org/abs/2311.14065.

[20] O. Quevedo-Teruel *et al.*, "Geodesic lens antennas for 5g and beyond," *IEEE Communications Magazine*, vol. 60, pp. 40–45, 1 Jan. 2022, ISSN: 15581896. DOI: 10.1109/MCOM.001.2100545.

[21] Y. Cai *et al.*, "Design of broadband low-profile transmitarrays at ka-band with high-permittivity 3d-printed materials," *IEEE Transactions on Antennas and Propagation*, 2025, ISSN: 15582221. DOI: 10.1109/TAP.2025.3597360.

[22] G. T. Chen, Y. C. Jiao, and G. Zhao, *Novel wideband metal-only transmitarray antenna based on 1-bit polarization rotation element*, Nov. 2020. DOI: 10.1002/mmce.22388.

[23] Z. J. Yang, R. Jiang, X. Zhuo, Y. M. Xie, J. Wang, and H. Q. Lin, *Dielectric nanoresonators for light manipulation*, Jul. 2017. DOI: 10.1016/j.physrep.2017.07.006.

[24] S. A. Matos, N. J. G. Fonseca, J. C. Serra, J. M. Felicio, J. R. Costa, and C. A. Fernandes, "Generalized risley prism for beam-steering transmit arrays with reduced grating lobes," *IEEE Transactions on Antennas and Propagation*, vol. 71, pp. 8420–8428, 11 Nov. 2023, ISSN: 0018-926X. DOI: 10.1109/TAP.2023.3313230. [Online]. Available: https://ieeexplore.ieee.org/document/10251119/.

[25] N. Zhang, W. X. Jiang, H. F. Ma, W. X. Tang, and T. J. Cui, "Compact high-performance lens antenna based on impedance-matching gradient-index metamaterials," *IEEE Transactions on Antennas and Propagation*, vol. 67, pp. 1323–1328, 2 Feb. 2019, ISSN: 0018926X. DOI: 10.1109/TAP.2018.2880115.

[26] P. Naseri, S. A. Matos, J. R. Costa, C. A. Fernandes, and N. J. G. Fonseca, "Dual-band dual-linear-to-circular polarization converter in transmission mode application to K/Ka band satellite communications," *IEEE Transactions on Antennas and Propagation*, vol. 66, pp. 7128–7137, 12 Dec. 2018, ISSN: 0018-926X. DOI: 10.1109/TAP.2018.2874680. [Online]. Available: https://ieeexplore.ieee.org/document/8486985/.

[27] M. Albani, G. L. Cono, R. Gardelli, and A. Freni, "An efficient full-wave method of moments analysis for RLSA antennas," *IEEE Transactions on Antennas and Propagation*, vol. 54, pp. 2326–2336, 8 Aug. 2006, ISSN: 0018926X. DOI: 10.1109/TAP.2006.879197.

[28] F. da Graça Gordo Cesar de Faria, "User terminal planar antennas for wireless broadband access at ka satellite band," Supervisors: Carlos A. C. Fernandes and Sergio A. Matos, Master's Thesis, Instituto Superior Técnico, Universidade de Lisboa, Lisboa, Portugal, 2021.

[29] K. Iqbal and Q. U. Khan, "Review of metasurfaces through unit cell design and numerical extraction of parameters and their applications in antennas," *IEEE Access*, vol. 10, pp. 112 368–112 391, 2022, ISSN: 21693536. DOI: 10.1109/ACCESS.2022.3214319.

[30] Y. Chen, Y. W. Mai, and L. Ye, *Perspectives for multiphase mechanical metamaterials*, May 2023. DOI: 10.1016/j.mser.2023.100725.

[31] A. Valipour, M. H. Kargozarfard, M. Rakhshi, A. Yaghootian, and H. M. Sedighi, "Metamaterials and their applications: An overview," *Proceedings of the Institution of Mechanical Engineers, Part L: Journal of Materials: Design and Applications*, vol. 236, pp. 2171–2210, 11 Nov. 2022, ISSN: 20413076. DOI: 10.1177/1464420721995858.

[32] M. Askari *et al.*, "Additive manufacturing of metamaterials: A review," *Additive Manufacturing*, vol. 36, p. 101 562, 2020. DOI: 10.1016/j.addma.2020.101562. [Online]. Available: https://doi.org/10.1016/j.addma.2020.101562.

[33] G. Lovat, P. Burghignoli, F. Capolino, and D. R. Jackson, "Combinations of low/high permittivity and/or permeability substrates for highly directive planar metamaterial antennas," *IET Microwaves, Antennas and Propagation*, vol. 1, pp. 177–183, 1 Feb. 2007, ISSN: 17518725. DOI: 10.1049/iet-map:20050353.

[34] B. Song, S. Zhang, L. Zhang, and Y. Shi, "Development trends and challenges of additive manufacturing metamaterials," *Engineering*, 2024. DOI: 10.1016/j.eng.2024.11.014. [Online]. Available: https://doi.org/10.1016/j.eng.2024.11.014.

[35] K. S. Prakash, T. Nancharaih, and V. S. Rao, "Additive manufacturing techniques in manufacturing-an overview," *Materials Today: Proceedings*, vol. 5, no. 2, pp. 3873–3882, 2018.

[36] S. A. Matos *et al.*, "3d-printed transmit-array antenna for broadband backhaul 5g links at v band," *IEEE Antennas and Wireless Propagation Letters*, pp. 1–1, 2020, ISSN: 1536-1225. DOI: 10.1109/LAWP.2020.2985399. [Online]. Available: https://ieeexplore.ieee.org/document/9057602/.

[37] F. Wei, J. W. Hao, L. Xu, and X. Shi, "A circularly polarized 3-d printed dielectric transmitarray antenna at millimeter-wave band," *IEEE Antennas and Wireless Propagation Letters*, vol. 20, pp. 1264–1268, 7 Jul. 2021, ISSN: 15485757. DOI: 10.1109/LAWP.2021.3077290.

[38] A. Massaccesi *et al.*, "3d-printable dielectric transmitarray with enhanced bandwidth at millimeter-waves," *IEEE Access*, vol. 6, pp. 46 407–46 418, Aug. 2018, ISSN: 21693536. DOI: 10.1109/ACCESS.2018.2865353.

[39] H. Yi, S. W. Qu, K. B. Ng, C. H. Chan, and X. Bai, "3-d printed millimeter-wave and terahertz lenses with fixed and frequency scanned beam," *IEEE Transactions on Antennas and Propagation*, vol. 64, pp. 442–449, 2 Feb. 2016, ISSN: 0018926X. DOI: 10.1109/TAP.2015.2505703.

[40] A. E. Mahmoud, W. Hong, Y. Zhang, and A. Kishk, "W-band mutlilayer perforated dielectric substrate lens," *IEEE Antennas and Wireless Propagation Letters*, vol. 13, pp. 734–737, 2014, ISSN: 15361225. DOI: 10.1109/LAWP.2014.2316144.

[41] X. Liu *et al.*, "Ultrabroadband all-dielectric transmitarray designing based on genetic algorithm optimization and 3-d print technology," *IEEE Transactions on Antennas and Propagation*, vol. 69, pp. 2003–2012, 4 Apr. 2021, ISSN: 15582221. DOI: 10.1109/TAP.2020.3026922.